3 Instrumental Capabilities

3.1 Introduction

3.1.1 ISS and JEM

3.1.1.1 Overall Structure

The Japanese Experiment Module (JEM), also known by a Japanese nickname *Kibo*, is the segment of ISS developed by the National Space Development Agency (NASDA) of Japan for supporting research and development experiments in the ISS orbit. The JEM consists of manned Pressurized Module (PM), Experiment Logistic Module-Pressurized Section (ELM-PS), and Exposed Facility (EF). The JEM Exposed Facility (EF), an unpressurized pallet structure exposed to the space environments, will be located just outside of the JEM Pressurized Module (PM) placed at the ram-port side of the ISS. The SMILES payload will be attached to the ram side of the JEM-EF at the location EFU #1 or EFU #3 as shown in Figure 3.1 and Figure 3.2.

3.1.1.2 Orbit and Attitude

The ISS will be in a nearly circular orbit at a nominal altitude of approximately 400 km with an inclination of 51.6 degrees to the equator, and will usually maintain a torque equilibrium attitude (TEA) during the microgravity mode of its operation. It is predicted that the ISS altitude will vary between 350 km and 460 km. In order to keep this altitude range, the ISS will be periodically reboosted approximately every 10 to 45 days by using onboard thrusters. During this Reboost Mode, the ISS attitude will be yaw-maneuvered by 180 degrees.

The ISS flight attitude (orientation relative to the plane of its orbit) is referenced to local-vertical/local-horizontal (LVLH) axes fixed with respect to the ISS's near-circular orbit [*NASA*, 1999]. The torque equilibrium attitude (TEA), which balances the average external torque disturbances such as aerodynamic torque and gravity gradient, will vary around the local-vertical/local-horizontal (LVLH) coordinate as shown in Figure 3.1. The x-axis points along the orbital velocity vector (the ram direction) and the z-axis points radially toward the Earth's center (or toward the nadir direction.) The ISS attitude variation will never exceed ± 15 degrees in roll and yaw angles and $+15$ and -20 degrees in pitch angle from the nominal LVLH attitude. The detailed descriptions of the orbit and attitude variations will be found in 3.2.5.

3.1.1.3 ISS Operational Modes

The ISS will be operated according to a number of specific modes of operation, each of which has a specified set of conditions and capabilities. Currently defined operation modes include Standard mode, Reboost mode, Microgravity mode, Survival mode, Proximity-Operations mode, Assured-Safe-Crew-Return mode, and External-Operations mode. Although most modes support research payload operations at some level, there are some modes for which payloads operations may be sharply curtailed or discontinued. Microgravity and Standard modes are the primary modes of operation during which full support for research payload will be provided. During Microgravity mode the ISS must be operated so as to meet a stringent set of requirements for its microgravity environment maintaining

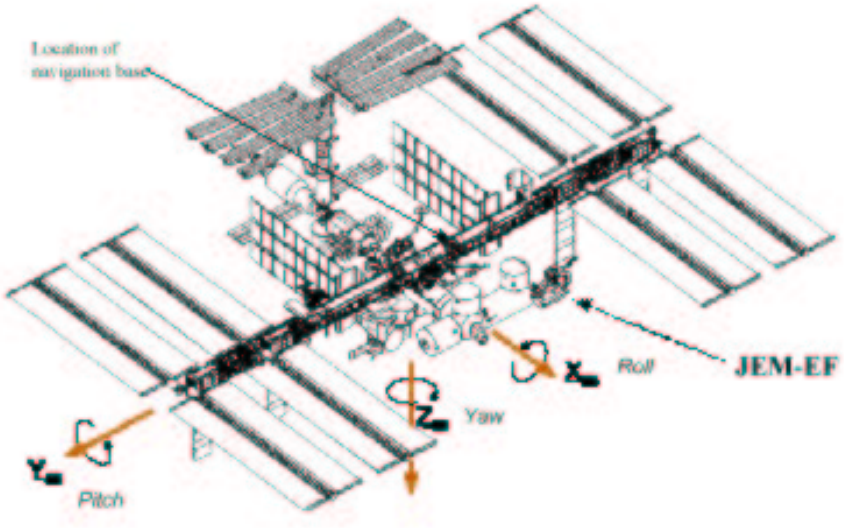

Figure 3.1 Space Station reference coordinate system. The x-axis points along the orbital velocity vector (the ram direction), the z-axis points radially toward the Earth's center (or toward the nadir direction).

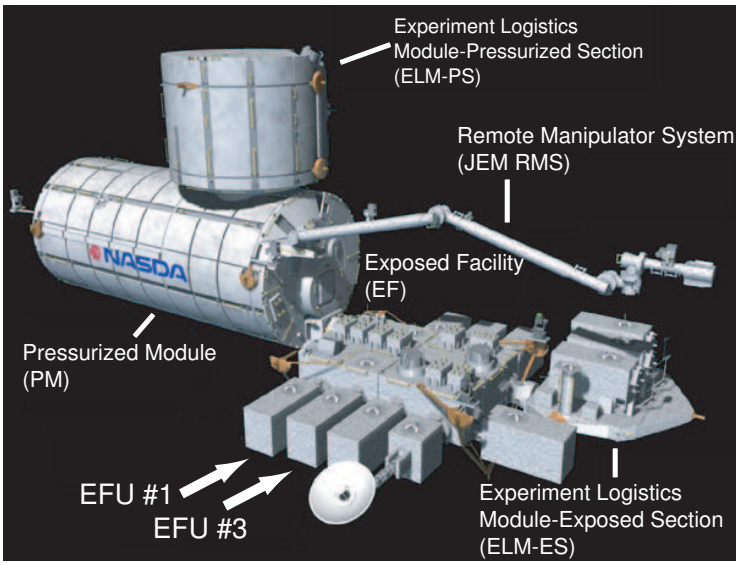

Figure 3.2 Configuration of Japanese Experiment Module (JEM). SMILES will be attached at the location EFU #1 or EFU #3

its attitude by non-propulsion means. Standard mode is similar to Microgravity mode except that microgravity environment will not be guaranteed.

In Reboost mode, drastic variations of altitude and attitude due to maneuvering will be expected. A periodic reboosting of the ISS will be carried out approximately every 10 to 45 days as described in 3.1.1.2. During Survival mode which will be invoked for the case of contingency, support and commanding for research payload are precluded. In these two

modes of operation, atmospheric observation by SMILES cannot be carried out.

In the remaining three modes of operation, Proximity-Operations, Assured-Safe-Crew-Return, and External-Operations, it is still not certain to what extent the SMILES atmospheric observations can be properly performed.

3.1.1.4 Data Link between JEM/SMILES and ground facility

Three types of data communications links are provided by the ISS for onboard data communications [*NASA*, 1999]: 1) a MIL-STD-1553B Payload Bus, 2) an IEEE 802.3 Ethernet, and 3) a fiber-optic High-Rate Data Link (HRDL). Among them, SMILES will employ the Payload Bus #2 for commanding and transmission of health-and-status (H&S) and house-keeping (HK) data of instruments, and the Ethernet for transmission of observation data as well as the instrument HK data.

There are two data links either through the U.S. Tracking and Data Relay Satellite System (TDRSS) or through the Japanese Data Relay Test Satellite System (DRTSS) are available for command uplink and data downlink between the ISS and the ground facilities at Tsukuba Space Center (TKSC) [*NASDA*, 1998]. Considering the resource allocation among International Partners for the TDRSS link, SMILES will only use the Japanese DRTSS link for which NASDA is allocated 50 % of link capacity. Although two DRTSs (DRTS-W and DRTS-E) are planned, only one DRTS (DRTS-W) will be available at the time of SMILES launch. Since the DRTS is an geostationary satellite, the DRTS link is secured only for a limited percentage of time during which it is visible from the ISS. During the loss-of-sight period referred to as Zone of Exclusion (ZOE), downlink data will be temporally stored in the High Rate Data Recorder (HRDR) with a capacity of 20 Gbits of the Interorbit Communication System (ICS) of JEM. Currently, downlink data rate available to SMILES is estimated to be 200 kbps at the most.

3.1.2 SMILES Payload

3.1.2.1 Payload Configuration

SMILES payload instrument consists of a number of sections as listed in Table 3.1. Figure 3.3 shows a block-diagram of SMILES payload instrument. The Submillimeter Antenna (ANT), Submillimeter Receiver (SRX), Intermediate Frequency Amplification Section (IFA), and Radio Spectrometer (AOS) comprises the main part of the payload. The Star Tracker (STT) has a function of detection and calibration of the SMILES payload attitude.

The SMILES is equipped with a heterodyne superconductor-insulator-superconductor (SIS) receiver to be operated in the 625/650-GHz band as a limb-emission sounding radiometer. The SMILES has a mechanically scanning elliptical offset-Cassegrain antenna with diameters of 40 cm × 20 cm to achieve an altitude resolution of about 3.5—4.1 km at the tangential altitude ranging from upper troposphere (10 km) to lower mesosphere (60 km) from the orbit of the ISS. The atmospheric limb emission collected by the ANT is directed to the SRX, where the received submillimeter-wave signal is combined with a reference signal (637.32 GHz) from a submillimeter-wave local oscillator (SLO), and is directed to SIS mixers through quasioptics consisting of focusing mirrors, wire-grids, and a sideband filter. Two SIS mixers, one of which for upper sideband (USB: 649.12 GHz – 650.32 GHz) and the other for lower sideband (LSB: 624.32 GHz – 626.32 GHz), are operated for simultaneously down-converting both sidebands into the intermediate frequency

Table 3.1 Configuration of SMILES Payload.

Section	Subsystem Components
Submillimeter Antenna (ANT)	Antenna Reflectors (REF)
	Antenna Mounting Structure (MNT)
	Beam Transfer Section (TRN)
	Cold-sky Terminator (CST)
	Antenna Drive Electronics (ADE)
	Calibration Hot Load (CHL)
Submillimeter Receiver (SRX)	Ambient Temperature Optics (AOPT)
	Cryo-electronics Unit (CRE)
	Ambient Temperature Amplifiers (AAMP)
	Helium Gas Compressors (HECP)
	Submillimeter LO Controller (SLOC)
	CRE Control Electronics (CREC)
	Stirling & JT Drive Electronics (SJTD)
IF Amplification Section (IFA)	
Radio Spectrometer (AOS)	AOS Analyzer Unit (AU)
	AOS Control & Video Unit (CVU)
Star Tracker (STT)	STT Camera Units (CAM)
	STT Camera Controller (CAMC)
Data Processing and Control Section (DPC)	
Payload Bus (BUS)	Electric Power System (EPS)
	Mainframe Structure (MFS)
	JEM Interface Mechanism (JIF)
	Thermal Control System (TCS)

(IF) band ranging between 11 GHz and 13 GHz. The IF signals are further down-converted and amplified in the IFA, and then analyzed by two acousto-optical spectrometers in the AOS. Further details of the functions of each subsystem will be described in the following sections.

3.1.2.2 Dimension, Mass, Power, and Data Rate

Figure 3.1.2.1 shows an external view of the SMILES payload. The envelope of the SMILES payload mainframe structure has a dimension of 1.85 m $\times$ 1 m $\times$ 0.8 m. The total mass of the payload is less than 500 kg. The electrical power consumption of the payload is less than 900 W for normal operation.

As a data communications interface for commanding and telemetry, SMILES will use the MIL-STD-1553B Payload Bus #2 and the IEEE 802.3 Ethernet. Commands from the ground and the ancillary data such as the reference time data are transmitted to the DPC through the Payload Bus #2 via the JEM Control Processor (JCP) and the Payload Data Handling Unit (PDH) and are distributed to SMILES subsystems [*NASDA*, 1998].

The Health and Status (H&S) data and the experimental data of the subsystem instruments are collected by the DPC and are downlinked to the ground through the 1553B Payload Bus #2 via the PDH and the JCP. The instrument experimental data are down-

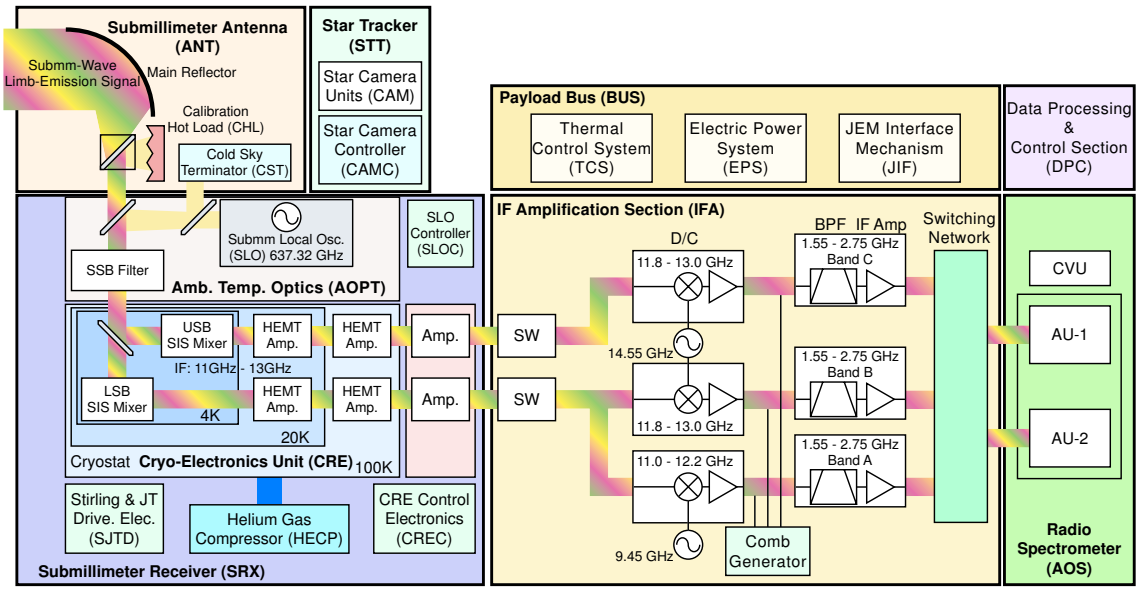

Figure 3.3 Block diagram of JEM/SMILES payload.

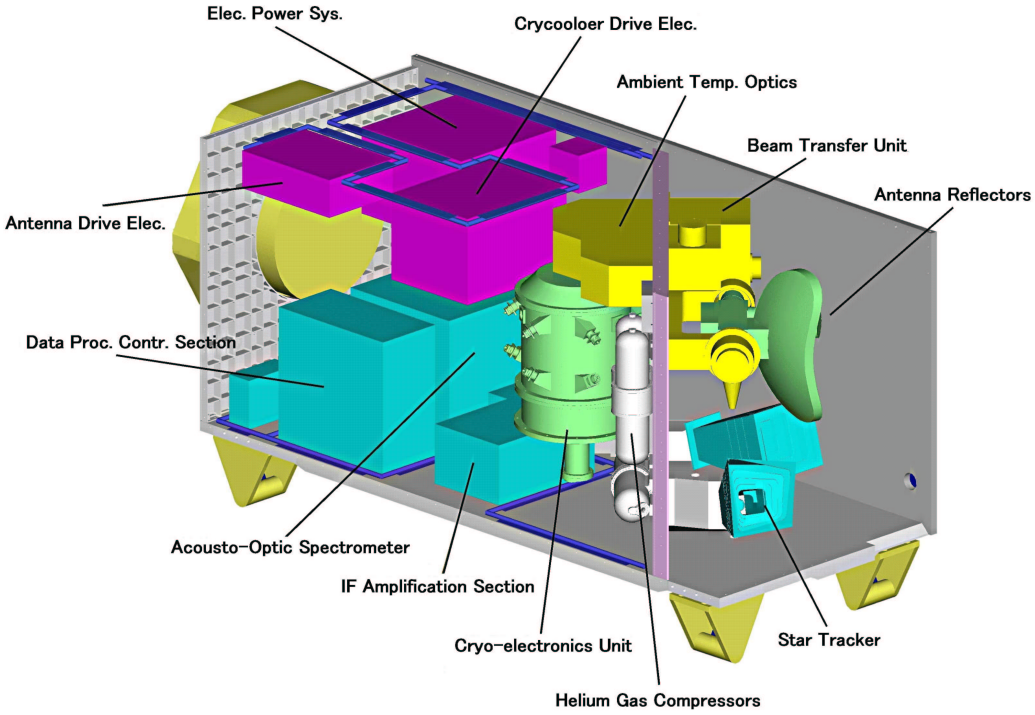

Figure 3.4 External view of the SMILES payload.

linked through the Ethernet along with the atmospheric observation data yielded by the AOS. The downlink 1553B data rate is estimated to be about 18 kbps which includes the H&S data of about 90 bps. The downlink Ethernet data rate is estimated to be less than

200 kbps.

3.1.2.3 Launching and Installation to JEM

SMILES will be launched around in 2007 by a Japanese H-IIA rocket from Tanegashima Space Center of NASDA in Japan. The SMILES payload will be transported to the orbit of the ISS by H-II Transfer Vehicle (HTV) and attached either to the JEM-EF Unit (EFU) #1 or #3. According to the current plan, on-orbit experiment mission period is scheduled to be one year. If there is no succeeding mission payload that takes place of the EFU position occupied by SMILES, the mission period of SMILES may be prolonged as long as the payload instruments are alive.

After the completion of its on-orbit mission, SMILES will be detached from the JEM-EF and thrown away into the atmosphere by HTV.

3.1.3 Mission Instruments

Mission instruments whose functions and performances are decisive to SMILES experiments comprise a submillimeter antenna, submillimeter receiver, intermediate frequency (IF) amplification section, radio spectrometer, star tracker, and data processing and control section. The following sections will give explanations and basic requirements for those instruments.

3.1.3.1 Submillimeter Antenna (ANT)

SMILES needs a submillimeter antenna that has a reasonable size and high degree of accuracy. Large mirror is preferable from the viewpoint of achieving a higher spatial resolution, particularly in the vertical direction. A kind of trade-off is, however, unavoidable over the spatial resolution and a given envelope for JEM payloads. Our choice is an elliptical mirror with dimensions of 40 cm in vertical direction and 20 cm in horizontal. The mirror is not so large, but it must be highly accurate in shape for generating a high-quality beam at submillimeter wavelengths. One important figure of merit is the beam efficiency, which represents how much radiation is collected in the main beam in comparison with inevitable sidelobe contributions. We regard a reasonable target for the beam efficiency is 90 % for the antenna alone, which means the efficiency in the case the antenna is illuminated by an ideal feed, and 85 % for the whole integrated SMILES system. In addition to these radio (optical) qualities, we need mechanical accuracies to determine the beam direction while the antenna is continuously driven along the atmosphere scan path. Since the vertical beam size is 0.09° (HPBW), the angular accuracy of the antenna driving mechanism must be better than 0.01°. The basic requirements on the antenna performance are summarized in Table 3.2.

3.1.3.2 Submillimeter Receiver (SRX)

A superconducting low-noise receiver is a key instrument of SMILES experiment. With SIS mixers associated with cryogenically cooled HEMT amplifiers, it will reduce receiver noise by a factor of 20 in comparison with the conventional semiconductor diode-mixer receiver. The SMILES receiver noise temperature will be about 500 K (SSB). Two SIS mixers, which are pumped by a single submillimeter LO source, will receive the atmospheric signal in the upper sideband (USB) and lower sideband (LSB) separately: one for 649.12—650.32 GHz, and the other for 624.32—626.32 GHz. The LO frequency will be stabilized to 10^{-7} by

Table 3.2 Requirements for SMILES-ANT

Items	Requirements
Observation frequency	624.32 — 650.32 GHz
Main reflector aperture size	400 mm (El) × 200 mm (Az)
Main beam width	0.09° (El) × 0.18° (Az)
Main beam efficiency	Higher than 90 %
Reflection loss	Higher than 50 dB
Elevation angle range	−40° to +5°
Elevation angle control accuracy	±0.01°

means of a phase-locked loop. A quasi-optical sideband filter, based on a modified Martin-Puplett interferometer, makes each SIS mixer sensitive to the atmospheric emissions only in one sideband, with suppression of more than 15 dB over the other sideband. A 4-Kelvin class mechanical cooler is another key component of SMILES. A combined system of a two-stage Stirling cooler and Joule-Thomson circuit will cool SIS mixers and their associated optics to 4.5 K, first HEMT amplifiers to 20 K and second HEMT amplifiers to 100 K. All the cooled components are contained in a cryostat that is thermally isolated from the ambient temperatures. The coolers are continuously operated with pressurized He gas supplied by compressors. The cooler lifetime will be determined by either residual mechanical abrasion or He gas deterioration due to outgassing. Current estimate of life is one year or longer. Basic requirements on the submillimeter receiver are summarized in Table 3.3.

Table 3.3 Requirements for SMILES-SRX

Items	Requirements
Input Frequency	624.32—626.32 GHz (channel-T)
	649.12—650.32 GHz (channel-R)
Image Rejection Ratio	More than 15 dB
LO Frequency	637.32 GHz
LO Frequency Accuracy	±64 kHz
LO Phase Noise	Lower than −75 dBc/Hz (offset 1 MHz)
Output Frequency	11.00—13.00 GHz (channel-T)
	11.80—13.00 GHz (channel-R)
Gain Linearity	±1% or less
Gain Variation	$3\%_{p-p}$ or less in 1 minute
Receiver Noise Temperature	500 K or less

3.1.3.3 IF Amplification Section (IFA)

IFA has functions of frequency down conversion and signal transmission from SRX to AOS. Since SMILES has three RF observation bands (Band-A and Band-B in LSB, and Band-C in USB), and two AOS units, it makes simultaneous observations only for two bands among three. So IFA should have functions of flexible combinations among these inputs and outputs, which is required from operational points of view as well as to prepare a kind of redundancy for reliability. IFA also contains functions of adjusting the output

power level and of generating reference signals, a comb generator, for calibrating the AOS frequency drift. The basic requirements are given in Table 3.4.

Table 3.4 Requirements for SMILES-IFA

Items	Requirements
Input Frequency	11.00—13.00 GHz (Band-A & B)
	11.80—13.00 GHz (Band-C)
Output Frequency	1.55—2.75 GHz
LO Frequency Drift	100 kHz or less
Gain Ripple	2.0 dB_{p-p} or less in a signal band
Gain Variation	0.04 $dB_{p-p}deg^{-1}$ or less
Comb Generator Frequency Step	100 MHz
Comb Generator Frequency Drift	17 kHz or less

3.1.3.4 Radio Spectrometer (AOS)

SMILES adopts the acousto-optical spectrometer (AOS) for analyzing the atmospheric signal and detecting its power spectrum. AOS will have two analyzing units, each of which has a frequency coverage of 1.55—2.75 GHz with a resolution of 1.8 MHz (FWHM) and each power spectrum is obtained with a CCD array of 1728 channels. The CCD data is digitized, accumulated and sent to DPC in every 1 sec. The basic requirements are given in Table 3.5.

Table 3.5 Requirements for SMILES-AOS

Items	Requirements
Input Frequency	1.55—2.75 GHz
Frequency Resolution	1.8 MHz or less (FWHM)
CCD: Number of Channels	1728 channels / each CCD
CCD: Channel Separation	0.8 MHz or less
Noise Dynamic Range	9 dB or more (for 10 % additional noise)
A/D Conversion Accuracy	12 bits
A/D Differential Nonlinearity	$\pm 1/2$ LSB or less
Data Accumulation	500 ms
Output Data Length	16 bits
Output Data Rate	108 kbps

3.1.3.5 Star Tracker (STT)

Since the ISS or JEM attitude is assumed to be unstable, SMILES will be equipped with two STT cameras to determine its real time attitude. Each camera will work unless the sun comes within an angular distance of 30°. STT will determine the attitude of the SMILES mainframe structure with respect to the stellar inertia coordinate. It is then converted to the attitude with respect to the coordinate fixed to the Earth to calculate the position of the tangential point of the SMILES beam. The basic requirements for STT are listed in Table 3.6.

Table 3.6 Requirements for SMILES-STT

Items	Requirements
Stellar Detection Limit	6.5 mag.
Attitude Determination Accuracy	0.003° (rms) for pitch, yaw
	0.03° for roll
	±0.03° for bias component
Attitude Refresh Period	0.96 s
Allowable Attitude Change Rate	$0.6°s^{-1}$
Solar Avoidance Angle	30° (separation from the STT axis)
Field of View	$18.4° \times 13.4°$
Reference Stellar Catalogue	Hipparcos Catalogue

3.1.3.6 Data Processing and Control Section (DPC)

DPC will have the following functions:

- to control the antenna scan, which is to be synchronized with IFA, AOS and STT,
- to acquire observation data from AOS and STT,
- to acquire telemetry data from almost all components of SMILES,
- to send necessary commands to SMILES components,
- to have data interfaces with ISS/JEM.

3.2 Field of View (FOV)

3.2.1 Altitude Scanning of the Antenna

3.2.1.1 Scanning Profile

The antenna scanning profile of SMILES is shown in Figure 3.5. Although the altitude and attitude of the ISS (and also SMILES) will vary during a mission life, a scanning profile of the antenna can be defined in terms of the relative elevation angles. A repetition period of the antenna scan is designed to be 53 seconds, the first 29.5 seconds of which are allocated to observations toward limb directions. The rest of the scan period is dedicated to calibrations for the system gain and the AOS frequency. The former is done firstly by directing the main reflector to a reference sky, at the altitude higher than 160 km, and secondly by inserting a calibration hot load (CHL) into the antenna submillimeter optics. A switching mirror is used for this operation. Frequency scale of the AOS is calibrated with a set of carrier signals injected into the IF band. The antenna scanning and the data accumulation in the AOS have to be synchronized by a SYNC pulse provided from the SMILES Data Processing and Control Section (DPC) with the accuracy of 1 ms.

3.2.1.2 Range of Tangent Point Altitude

The height of tangent point for a line-of-sight depends on the antenna elevation angle as well as the altitude and attitude of the ISS/SMILES. Precise direction of the submillimeter beam will be determined with a reference to the Star Tracker (STT) data in the Level-1 data processing on the ground. In orbit, however, the prediction errors and fluctuations of

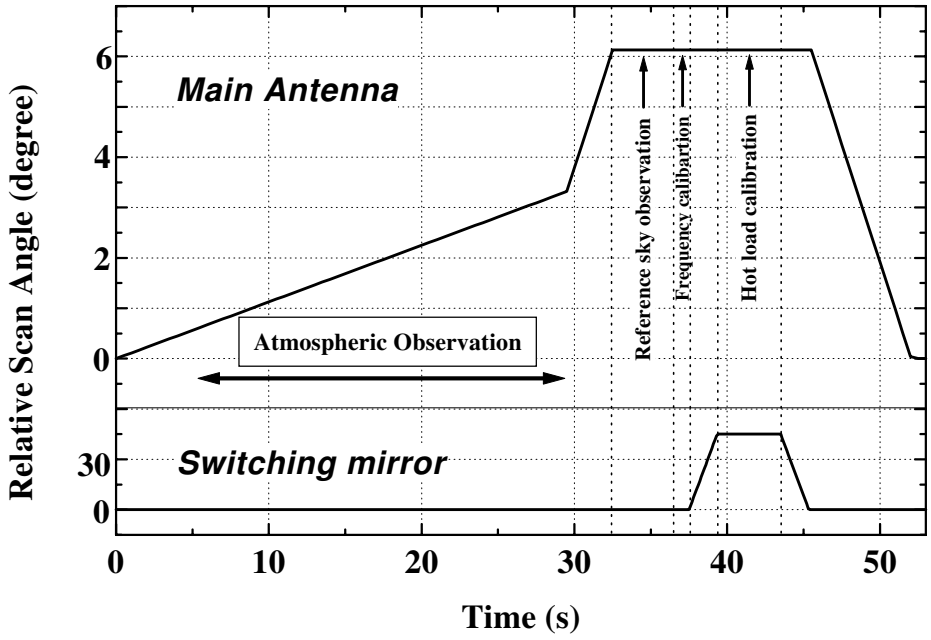

Figure 3.5 Antenna scanning pattern of SMILES with the associated operation of a switching mirror for radiometric calibration.

the ISS attitude will bring a large uncertainty in the tangent point altitude. For simplicity of the system, we have designed the ascending phase wide enough to cover the altitude range of 10 to 60 km with a sufficient margin. Initial tangent point altitude of every scan is settled to a nominal value of −35 km on the basis of predicted information of the ISS orbit and attitude. An expected range of real observational altitudes is listed in Table 3.7 for several representative altitudes and attitudes of the ISS.

3.2.1.3 Spatial Sampling Rate and Altitude Resolution

During atmospheric observations in the scanning period, the antenna ascends at a stepping rate of 12 Hz with a unit angle of 0.009375°. The emissions from the limb-atmosphere are accumulated, or averaged, for 500 ms to generate a unit output data. Strictly speaking, six different emissions originating from six consecutive altitudes contribute to each spectrum data. The effective beam-size for such output spectrum is calculated to be 0.096° in HPBW. Both the beam size and sampling interval, expressed in altitude at the tangent point, depend on the altitude and attitude of the ISS. They also vary along the antenna scan, because the distance between the tangent point and the ISS decreases as we go to the higher tangent point altitude. Figures 3.7 and 3.8 shows how the beam size and sampling interval will change while the antenna is ascending in a single scan.

Table 3.7 Expected range of tangent point altitudes for several ISS conditions.

Roll (deg.)	Pitch (deg.)	Yaw (deg.)	ISS Altitude (km)	Obs. Range (km)	Reference Sky (km)
0	0	0	350	−35 - 84	168
0	0	0	400	−35 - 92.5	184
0	0	0	460	−35 - 102	201
*1 0.5	−8.8	−2.0	350	−35 - 83	167
*1 0.5	−8.8	−2.0	400	−35 - 91.5	182
*1 0.5	−8.8	−2.0	460	−35 - 101	200
*2 −15	−20	−15	350	−35 - 82.5	166
*2 −15	−20	−15	400	−35 - 91	181
*2 −15	−20	−15	460	−35 - 100	198
*3 15	15	15	350	−35 - 83.5	167
*3 15	15	15	400	−35 - 92	183
*3 15	15	15	460	−35 - 101	200

*1: Expected ISS attitude after FLT 15A (Rev.D) SMILES will be installed around this event. *2 and *3 : The worst case of the ISS attitude.

3.2.1.4 Reference-sky Calibration

Onboard calibration of the radiometric gain will be done with two noise references at submillimeter wavelengths; the hot-load (CHL) that is virtually a black-body at the ambient temperature, and the reference sky that can be regarded as the microwave cosmic background. The two references are measured by the SMILES receiver in every antenna scan. The reference sky is measured with the main reflector of the antenna that is set at 6.13° upward with respect to its initial position. As far as the initial antenna position is adjusted in every scan at the nominal altitude of −35 km, which is to be programmed based on the prediction of the ISS altitude and attitude, the real height of the reference sky will be higher than 160 km. Since SMILES observes at around 640 GHz, the brightness temperature, which usually expressed in the Rayleigh-Jeans temperature, of the cosmic background is virtually zero Kelvin.

For the hot load calibration, a switching mirror is inserted into the antenna optics for the SMILES receiver to view the CHL. The physical temperature of the CHL is measured with the accuracy of 0.1° every 10 seconds. Since the reflectivity of the CHL is well suppressed to −55 dB or less, its brightness temperature is also accurate. In the scan period of 53 seconds, we allocate 4 seconds each to the hot load and reference sky calibrations. This method makes the increase of spectral noise, which is attributed to the subtraction between the atmospheric and the reference sky data, to be less than 10 %.

3.2.1.5 Continuity of Observations

Once SMILES is launched and attached to the JEM-EF Unit, the first several weeks will be reserved for initial checkout of the instruments. During this period, electrical performance of the radiometer is optimized and the antenna pointing accuracy is established. During a mission life, several engineering tests will be scheduled to confirm operating conditions of the instruments. In addition to the engineering tests, several factors can prevent continuous observations:

1. Acute attitude changes of the ISS
   Among the ISS operational modes, Microgravity Mode is only suitable for limb sounding from the viewpoint of attitude stability. More than 30 successive days in one time and more than 180 days in total per year are planned to be in Microgravity Mode after completion of the ISS construction. During the construction phase of the ISS, the length of this mode will be shortened due to more flights accessing to the ISS. Observations can be continued during Standard Mode, if attitude changes are found not severe. Dynamical analysis of the SMILES attitude is still in progress.

2. Poor environmental conditions on the ISS
   RF electromagnetic fields radiated from transmitters on the ISS may deteriorate the quality of the observed spectra. Of course, in its current design, the SMILES instruments are well shielded against such harmful radiations by means of completely enclosed panels. The submillimeter receiver is also protected by the cryostat. In spite of that, some interference may remain on the observed spectra in the worst cases. The increase of the background pressure around the JEM also may limit normal operation of SMILES, because we have to protect cryogenically cooled components from contamination. This situation can occur in the events such as water dump from the Space Shuttle orbiter, the ISS boosting by a propulsion module, or ventilation from the pressurized module of the JEM.

3. Limitations on the ISS resources
   The ISS is a multi-purpose facility that accommodates many experiments in the same period. SMILES will be provided from the ISS-JEM with resources such as electric power, coolant, and means of data communications. When a large amount of electric power is needed for some other experiment on board, SMILES may be requested to reduce its power consumption. It is however impossible for SMILES to continue atmospheric observations with a reduced level of power consumption. On the other hand, heavy traffic in the ISS data link system may force SMILES to reduce its data generation. This also means that SMILES has to be dormant.

3.2.1.6 Effects of Atmospheric Refraction

So far the effects of refraction due to Earth's atmosphere on the limb-sounding field-of-view are ignored. For submillimeter-waves propagated in the actual Earth's atmosphere, the propagation path is deviated from the geometrical straight line due to refraction caused by vertical gradient of the refractive index which depends on the atmospheric pressure, temperature, and humidity.

Figure 3.6 shows the effects of refractive bending on the limb-sounding line-of-sight paths for two typical reference atmospheres, i.e., low-latitude annual and high-latitude-winter atmospheres[1]. It is found in Figure 3.6 that the refractive bending of the path gives rise to an appreciable deviation from the geometrically calculated one for the paths with tangent points below 20 km.

A significant deviation are found for the actual atmosphere below 15 km in tangent point altitude compared with the case of no refraction (Fig. 3.6). However, variations among different models of atmospheres, which representing seasonal changes, are almost negligible for altitudes above 2 km [*Manabe*, 2000]. The simple exponential model [*International Telecommunication Union*, 1997], in which the atmospheric refractivity n is given

[1]Further detailed discussions on the effects of atmospheric refraction on JEM/SMILES limb-sounding and their dependence on atmospheric models and on radiowave frequency, etc., are found elsewhere [*Manabe*, 1999; *Manabe*, 2000].

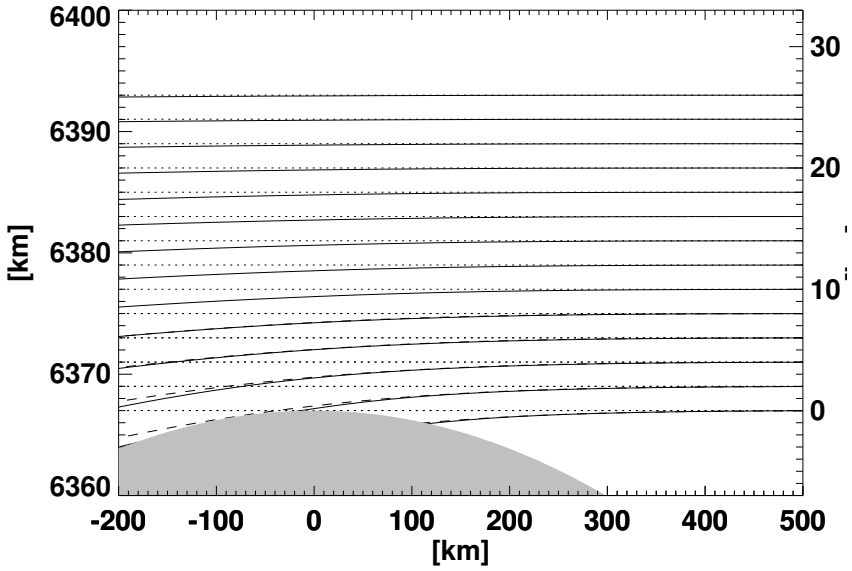

Figure 3.6 Effects of atmospheric refraction on limb-sounding line-of-sight paths for geometrical tangent height without refraction of every 2 km from 0 km to 26 km. Solid and dashed curves are calculated for the low-latitude-annual and high-latitude-winter reference atmospheres [*Manabe*, 2000; *International Telecommunication Union*, 1997], respectively, while the dotted line represents the geometrical ray without refraction. Although the ordinate is exaggerated about 10 times as the abscissa, geometrical rays without refraction are represented by straight lines. For the sake of clarity, nominal tangent points for refraction-free rays are aligned on $x = 0$ km. The SMILES orbital altitude is assumed to be 400 km.

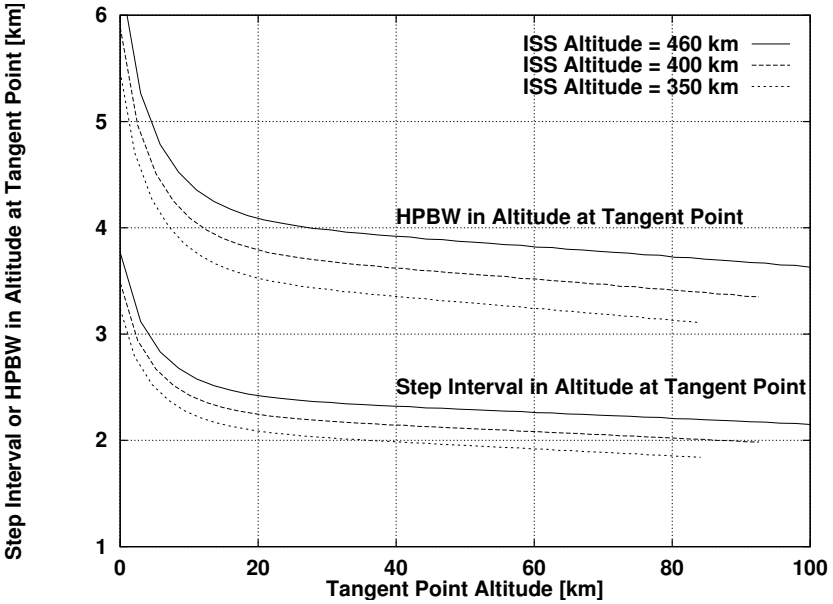

Figure 3.7 Antenna scanning step interval and vertical half-power beamwidth (HPBW) at tangent point for exponential model atmosphere for ISS orbital altitudes of 350 km, 400 km, and 460 km

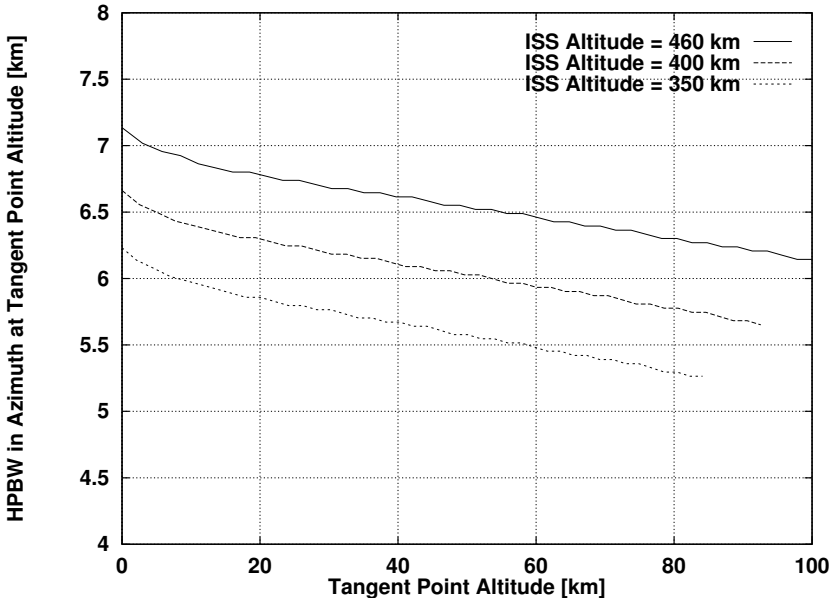

Figure 3.8 Horizontal half-power beamwidth (HPBW) at tangent point for exponential model atmosphere for ISS orbital altitudes of 350 km, 400 km, and 460 km

by a simple exponential function of altitude h [km] as

$$n(h) = 1 + 315 \times 10^{-6} \exp(-h/7.35), \tag{3.1}$$

is found to be a good approximation to a wide range of actual atmosphere.

As a result of the refractive bending of the limb-sounding path, the spatial resolution defined by the antenna beamwidth at the tangent point becomes slightly worse than is expected by ignoring atmospheric refraction. Figures 3.7 and 3.8 show the effects of atmospheric refraction on the spatial resolution at the tangent point calculated for the cases of ISS orbital altitude of 350 km, 400 km, and 460 km by assuming the exponential reference atmosphere whose altitude profile of atmospheric refractivity is given by Eq. (3.1) and the spherical Earth with a radius of 6378.136 km.

3.2.2 Global Coverage

3.2.2.1 Global Coverage of Atmospheric Limb Scanning

Since the ISS orbit is a circular orbit with an inclination of 51.6° to the equator, the highest latitude reached by the ISS orbit is 52° in north and south. In order to extend the latitudinal coverage to the north polar region where the ozone depletion is significant, the field-of-view of the SMILES antenna is deflected 45° to ram port side from the ISS orbital plane. SMILES limb-sounding observation with this field-of-view deflection provides a latitudinal coverage 65° N to 38° S on each orbit.

In Figure 3.9, red segments depict the ground projections of the tangent points for the altitude of 10 km to 60 km in the antenna scanning scheme described in 3.2.1. The associated one-day orbit, shown by a blue curve, is assumed to start from the ascending node in the prime meridian. Each red segment corresponds each limb scan from 10 km to 60 km in altitude. In this calculation, it is assumed that the Earth is spherical with a radius of 6378 km, the ISS travels at a speed of 7.669 km/s in a circular orbit with an

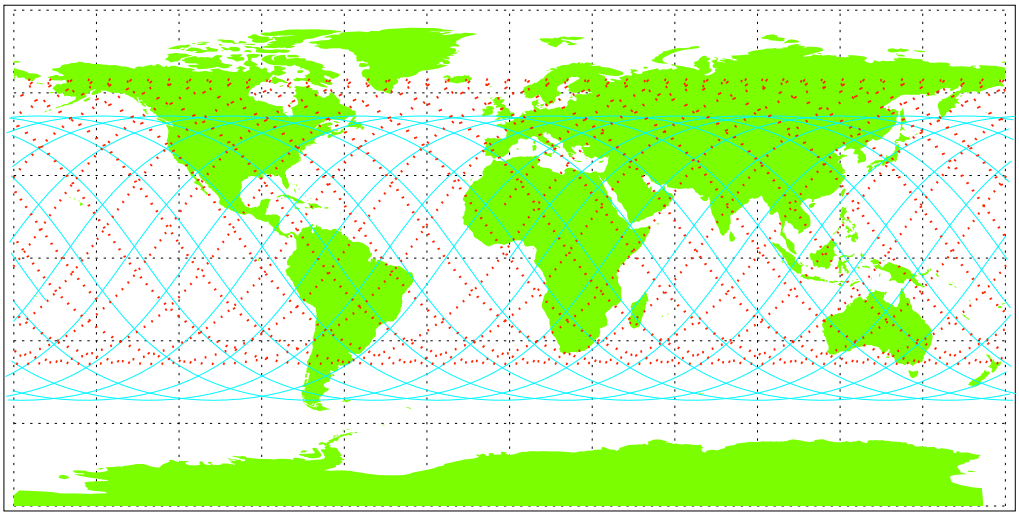

Figure 3.9 The SMILES observation tangent-point coverage (red dots) for an ISS one-day orbit starting from the ascending node corresponding to the prime meridian (blue curve). Only the tangent points within the altitude range between 10 km and 60 km are plotted. The earth is assumed to be spherical with a radius of 6378.136 km. The ISS orbital altitude is assumed to be 400 km. (Cylindrical equidistant projection)

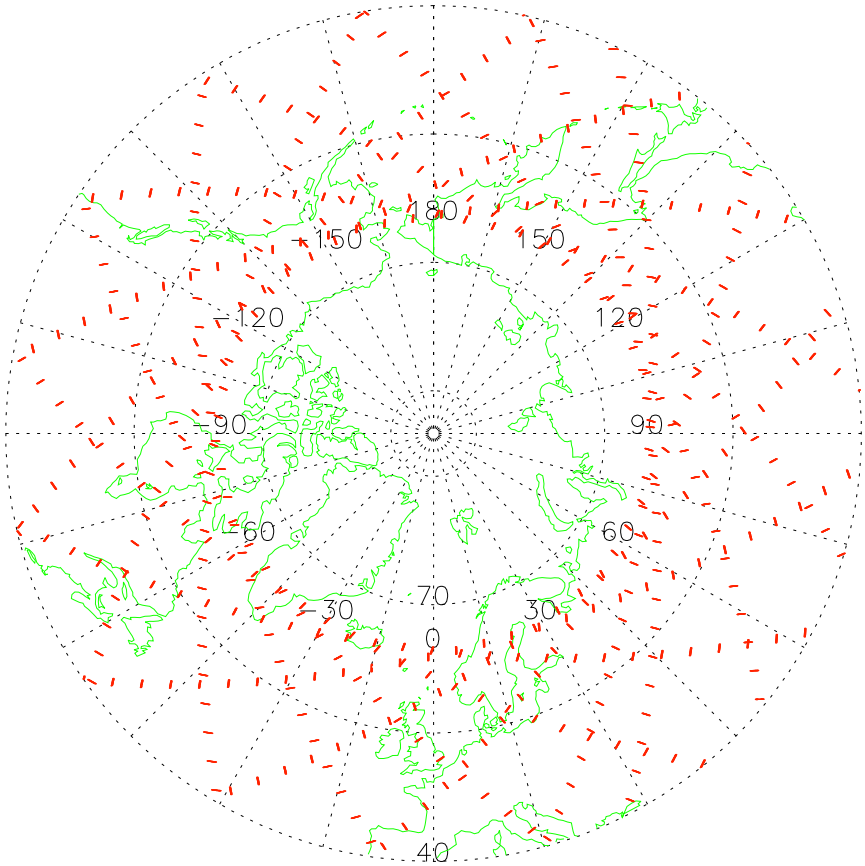

Figure 3.10 The SMILES observation tangent-points coverage (red dots) viewed from the north. (Azimuthal equidistant projection)

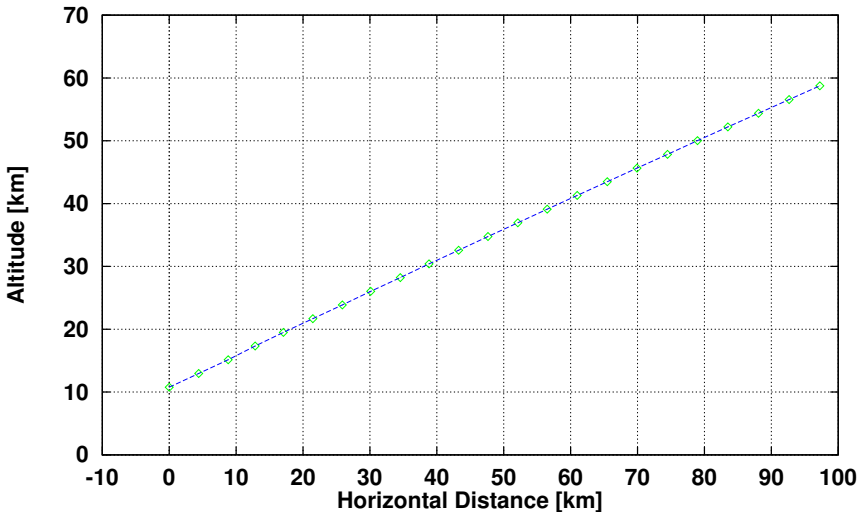

Figure 3.11 Trajectory of tangent points in a vertical plane for single limb scanning.

orbital altitude of 400 km. An along-track separation of about 360 km between adjacent limb scans, which corresponds to about 105 limb scans per orbit, can be achieved by the SMILES antenna scanning scheme described in 3.2.1. Figure 3.10 shows the coverage of the SMILES observation tangent points around the Arctic Circle. It is found in Figure 3.10 that the limb sounding by SMILES samples most densely the northern high latitude region around the 65° N parallel of latitude around which the polar vortex may appear.

Figure 3.11 shows the trajectory of the tangent points in the vertical plane for a limb scanning from 10 km to 60 km. For each limb scanning, the tangent point travels about 100 km in horizontal direction as its altitude increases from 10 km to 60 km[2]

3.2.2.2 Horizontal Resolution

In the retrieval of scientific parameters, the atmosphere should be assumed to be homogeneously stratified, i.e., the atmospheric properties depend only on the altitude. In Figure 3.12, the area where the horizontal homogeneity should be assumed is depicted by a right blue triangle for a single limb scan from 10 km to 60 km. The size of this triangle area is considered to be a measure of the horizontal resolution for single limb scanning. The base of this triangular area is about 1550 km irrespective of the ISS orbital position while its altitude varies within a range between 50 km and 57 km depending on the ISS longitude.

3.2.2.3 Effects of ISS Attitude and Altitude on Global Coverage

So far the attitude of ISS is assumed to be in the nominal LVLH attitude ignoring attitude variation. If the attitude variation of ±15° in yaw angle is taken into account, the latitudinal coverage should be between 68°N and 35°S for a −15° yaw deviation, and between 61°N and 42°S for a +15° yaw deviation (the yaw angle of the ISS is defined

[2]It should be noted that the effects of atmospheric refraction is ignored here. If the effects of atmospheric refraction are taken into account, horizontal extent of the tangent points for a shingle limb scanning becomes appreciably longer than 100 km. See http://www.crl.go.jp/ck/ck321/smiles/refrac/refrac.html, and http://www.crl.go.jp/ck/ck321/smiles/refrac/refrac.pdf.

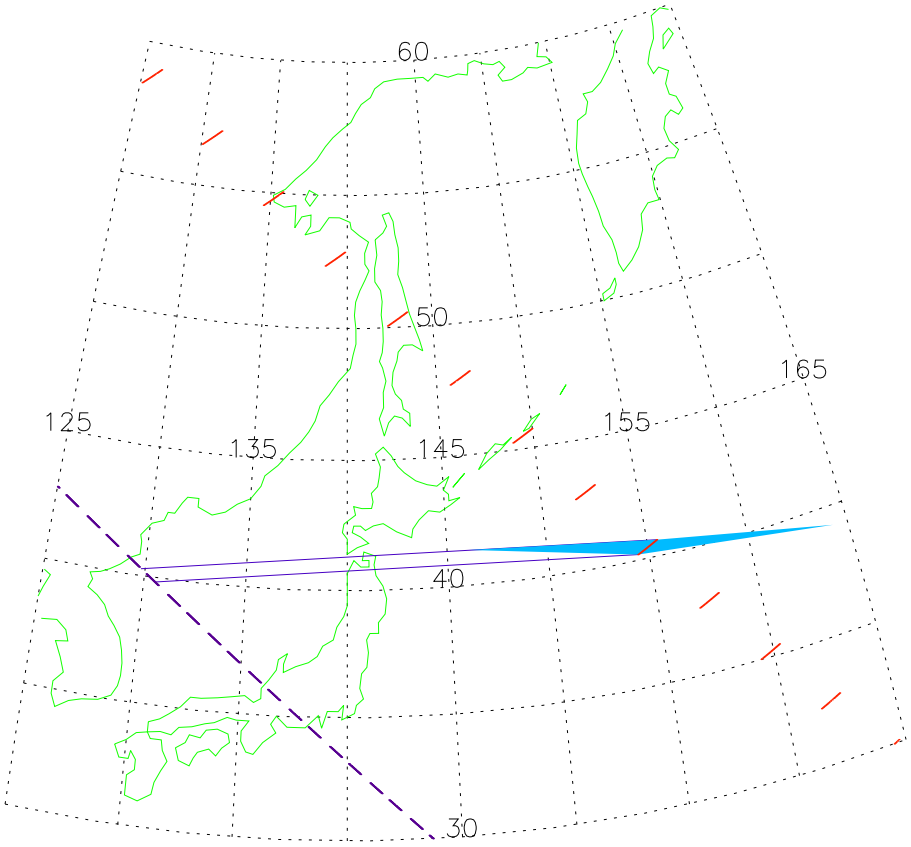

Figure 3.12 The horizontal resolution of SMILES observation depicted by a blue triangle defined as the area where the horizontal homogeneity should be assumed for limb sounding. Red segments are the ground projection of the trajectory of tangent points within a range between 10 km and 60 km. Broken line is a sub-orbital track of the ISS.

in Fig. 3.1) The effects of pitch and roll variations are trivial since the range of antenna elevation scanning has some margin for short-term small variations as described in 3.2.1.2 and can be offset for long-term large variations.

If the ISS altitude is within a range between 350 km and 460 km, its variation has smaller effects on the latitudinal coverage than the yaw variation. Highest latitudes covered by SMILES limb observations are summarized in Table 3.8 for several different combinations of the ISS altitude and yaw deviation. The highest latitude is defined here as the one reached by the 10-km altitude tangent point by SMILES limb observation.

Table 3.8 Highest latitudes sampled by SMILES limb scanning. Highest latitudes are defined as the highest latitude of the tangent point for altitude of 10 km reached by SMILES limb scanning

(a) Northern Hemisphere

	+15°	0°	−15°
460 km	61.9°N	66.2°N	69.6°N
400 km	61.2°N	65.3°N	68.4°N
350 km	60.6°N	64.4°N	67.4°N

(b) Southern Hemisphere

	+15°	0°	−15°
460 km	41.3°S	37.0°S	33.6°S
400 km	42.0°S	37.8°S	34.8°S
350 km	42.6°S	38.8°S	35.8°S

3.2.3 Interference with FOV

3.2.3.1 Interference by the Sun

Since the ISS orbit is sun-asynchronous, the incidence of solar radiation can be from any direction except that of the Earth. SMILES does not have an azimuthal drive of the main reflector, so that its main beam inevitably makes an occasional encounter with the sun. In that case, the SMILES receiver will suffer from about 10 times larger signal than the normal operation. SMILES will use a switching mirror to protect critical devices such as the Radio Spectrometer (AOS). Besides the main reflector, SMILES has the Cold-sky Terminator (CST) that sees the zenith. The CST is used as a low-temperature submillimeter-wave source for the image sideband of SIS mixers, so that the signal from the CST is always fed to the SMILES receiver on almost equal weight of intensity with the signal from the main reflector. Coaxial switches, denoted as 'sw' in Fig. 3.3, in the IF Amplification Section (IFA) will be turned off while solar radiation interferes with the CST beam.

The Data Processing and Control Section (DPC) will control these switching operations, following a programmed sequence. Because of the uncertainty of the ISS attitude, the duration of the switch-off mode must be longer than that expected only from the antenna beam-width. The frequency of interference by the sun in the main beam and the CST beam depends on the ISS orbit, season, latitude, and local time. The sun hits the main beam in the morning of a particular season depending on the latitude, while the sun comes to the zenith when the ISS flies over low latitudes around its local noon.

In Figure 3.13, the local times of the SMILES observation points are plotted with green dots in the latitude range of 0 - 10°N, 30 - 40°N, and 50 - 60°N. In this figure, red crosses show where the sun comes within ±2° from the line-of-sight of the main beam. The solar interference with the main beam occurs around 6 o'clock of local time in the season near equinox. In the same figure, the interference with the CST beam is shown with orange boxes. The points where the sun comes within ±3° from the ISS zenith are marked. This interference occurs at the local noon occasionally. Refer the caption of the figure for assumptions used in this calculation.

3.2.3.2 Interference by the Solar Paddle

While SMILES has an ability of dense observation in Arctic region, its main beam is occasionally interfered by the ISS solar paddles. The SMILES main beam views 45° north from the ISS orbital plane. The huge photovoltaic arrays, which rotate around the axis of the ISS main truss, will intersect the SMILES main beam twice an orbital rotation of the ISS (Figure 3.14). Blue circles in Fig. 3.13 plot the points where the photovoltaic arrays come within ±0.1° from the SMILES main beam. Averaged probabilities of the interference are 1.2%, 0.8%, and 0.5% in the latitude range of 0 - 10°N, 30 - 40°N, and 50 - 60°N, respectively. If we assume the main beam is interfered when the photovoltaic arrays come within ±1°, the probabilities increase. The probabilities of the occurrence of interference are shown in Fig. 3.15 for three different types of interferences described above. Local times when the interferences occur are unevenly distributed, in particular local noons have the higher probabilities of the interference as shown in Fig. 3.15.

3.2.4 Antenna Response Pattern

SMILES has a mechanically-scanning offset-Cassegrain antenna of 400 mm × 200 mm in diameter, which is designed to generate an elliptical beam with an altitude resolution of around 3.2-4.4 km at tangent altitudes ranging from 10 km to 60 km, while keeping the physical size small enough to be compatible with the payload envelope. The Half-power

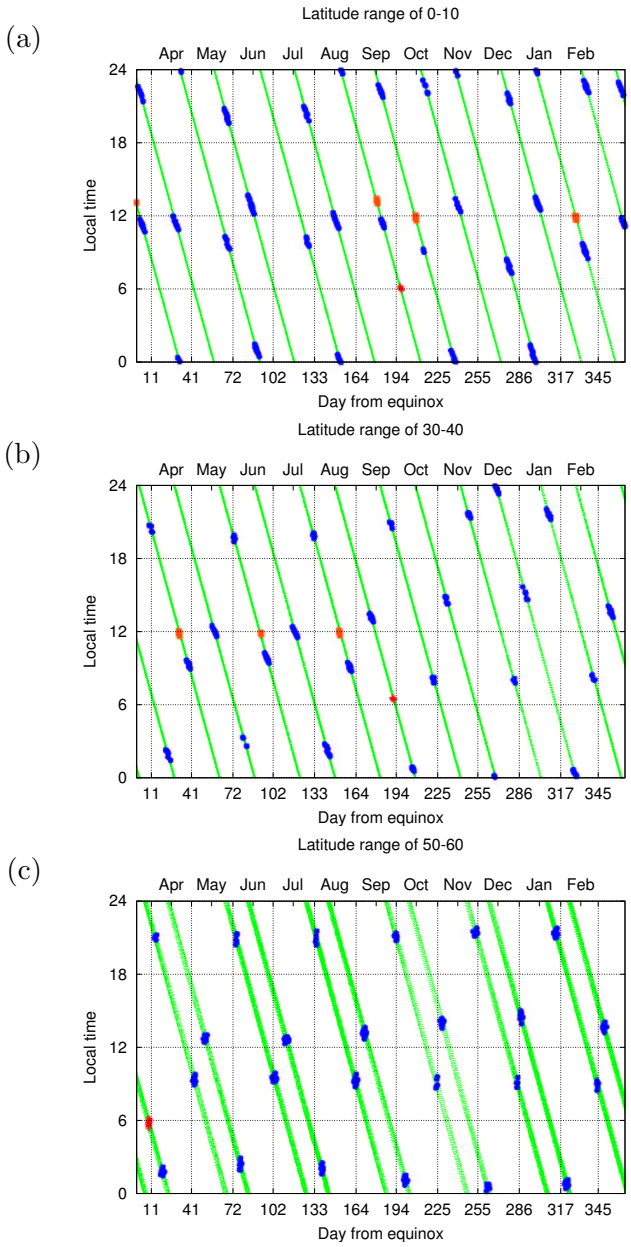

Figure 3.13 The local time of the SMILES measurements. The local times are shown (green dots) with respect to the day from the vernal equinox. The SMILES single scan is assumed to last 53 seconds. Green dots are replaced with other marks when one of the measurements in the scan has the solar interference with the main beam (red vertical crosses), or the CST beam (orange boxes), or the solar paddle interference with the main beam (blue circles). Three latitudinal zones are calculated; (a) 0 - 10°N, (b) 30 - 40°N, and (c) 50 - 60°N. Assumptions are; a circular orbit of the ISS, a spherical earth, the ISS decreasing altitude from 400 km to 386 km, a simple rotation of the ISS solar paddle pointing toward the sun, and the SMILES location of EFU #3 on JEM-EF. It is judged to be interfered when the interior angle between the sun and the main beam, the sun and the CST beam, and the nearest point of the solar paddles and the main beam are lower than 2°, 3°, and 0.1°, respectively.

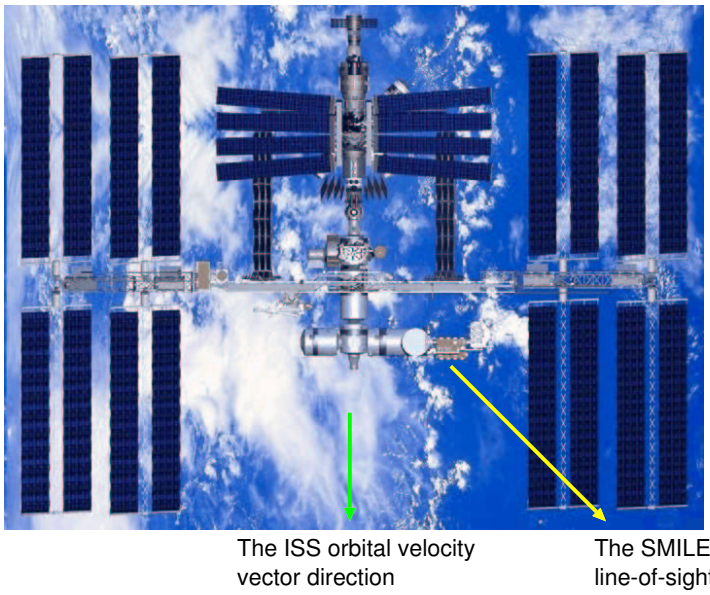

Figure 3.14 Top view of the ISS. The rotating solar paddle will occasionally intercept the SMILES main beam (yellow arrow).

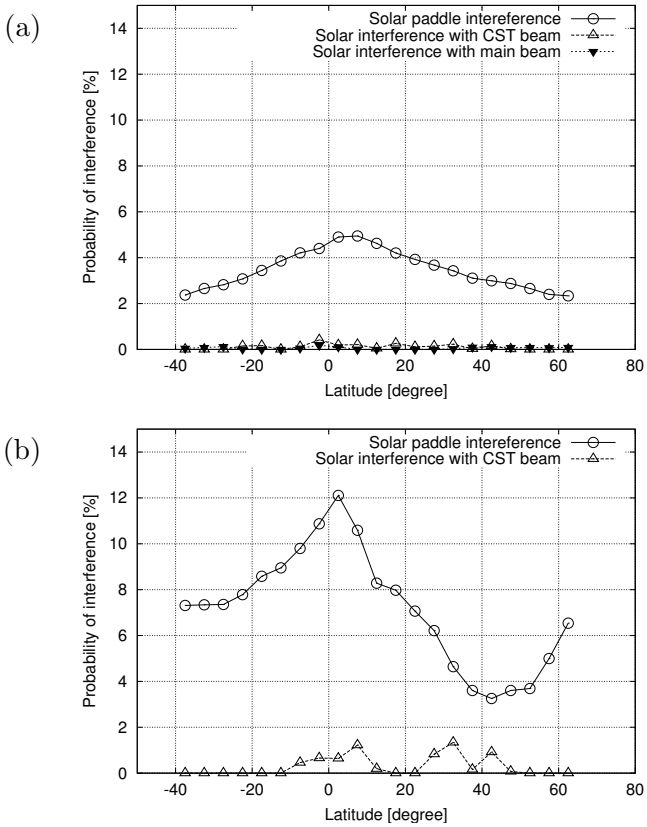

Figure 3.15 The probability of the interference versus latitude. Plotted are the ratios of the numbers of scan which include interfered measurements by the sun with the main beam (filled triangles) or with the CST beam (open triangles) or by the solar paddle with the main beam (circles) to the total number of scan. The ratios are calculated from (a) whole one year scans and (b) one year scans corresponding to local times between 9:00 and 13:00.

Table 3.9 Antenna Specification. * Frequency: 637.32 GHz. FOV beam efficiency is defined as the relative radiated power involved within a 2.5-time HPBW area.

Item	Characteristic
Antenna shape	Elliptical-beam offset Cassegrain
Aperture diameters	400 mm × 200 mm
Main reflector material	Aluminum with a sandblast treatment
Surface roughness of reflectors	5 μm rms
Surface accuracy of reflectors	15 μm rms
Aperture edge-level	-20 dB*
Beam width (HPBW$_{Az}$)	0.173°*
Beam width (HPBW$_{El}$)	0.083°*
FOV beam efficiency	Higher than 90 %*

specification of the SMILES antenna is summarized in Table 3.9.

A calculated near-axis response pattern of the SMILES antenna is shown in Figure 3.16 (designed by MELCO). The surface shape of the main- and sub-reflectors has been op-

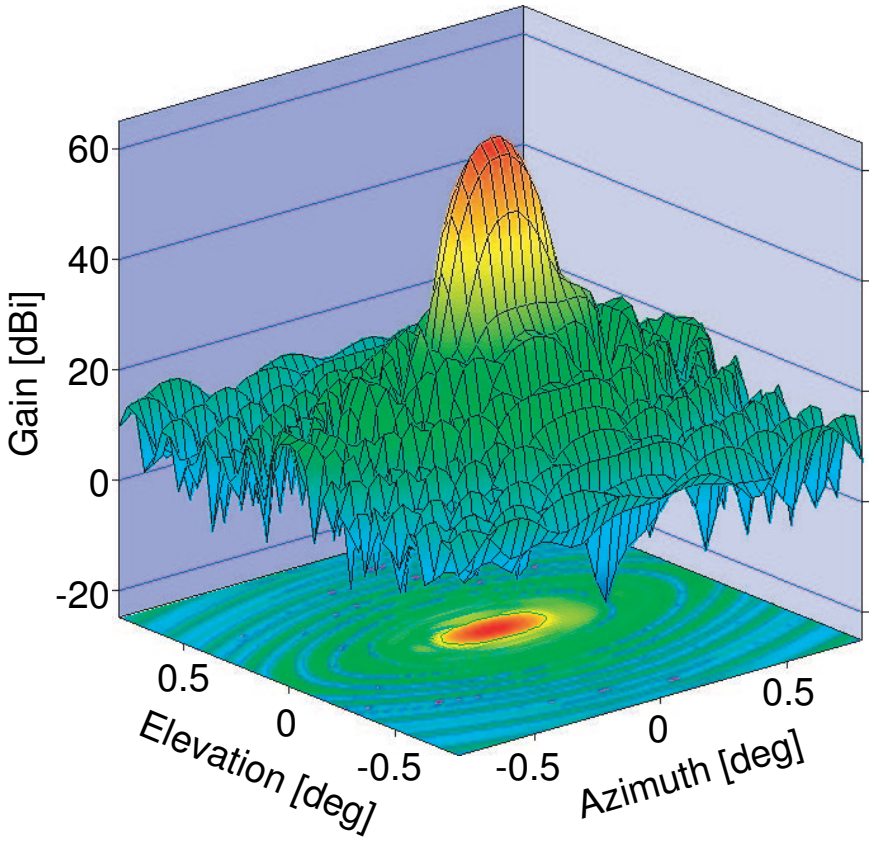

Figure 3.16 Calculated near-axis antenna response pattern.
(designed by MELCO)

timized for achieving low sidelobe levels and high beam efficiency. Such quality of the submillimeter beam is essential to reduce additional noise contributions from the earth and the SMILES payload itself. The actual response pattern of the antenna will be evaluated with a near-field phase-retrieval measurement on the ground.

3.2.4.1 Response Pattern Model

In order to evaluate the effect of the antenna response pattern on atmospheric limb scanning, we introduce an approximate response pattern model. An antenna response function is described as $P(Az, El)$.

The model is defined in four regions and consists of three functions as shown in Figure 3.17. Region A is an area to define the FOV beam efficiency. Region B represents a main beam area. Region A is within region B. A response pattern in regions A and B (P_{main}) is approximated by a gaussian function as following:

$$P_{\mathrm{main}}(Az, El) = 10 \log \left(a_0 + a_1 \exp \left(-\frac{1}{2} \left(\left(\frac{Az}{a_2} \right)^2 + \left(\frac{El}{a_3} \right)^2 \right) \right) \right) \ [\mathrm{dB}] \tag{3.2}$$

where Az and El is the azimuth and elevation angles in a coordinate fixed on the main reflector. Region C describes an error pattern area. In region C, a response pattern (P_{error})

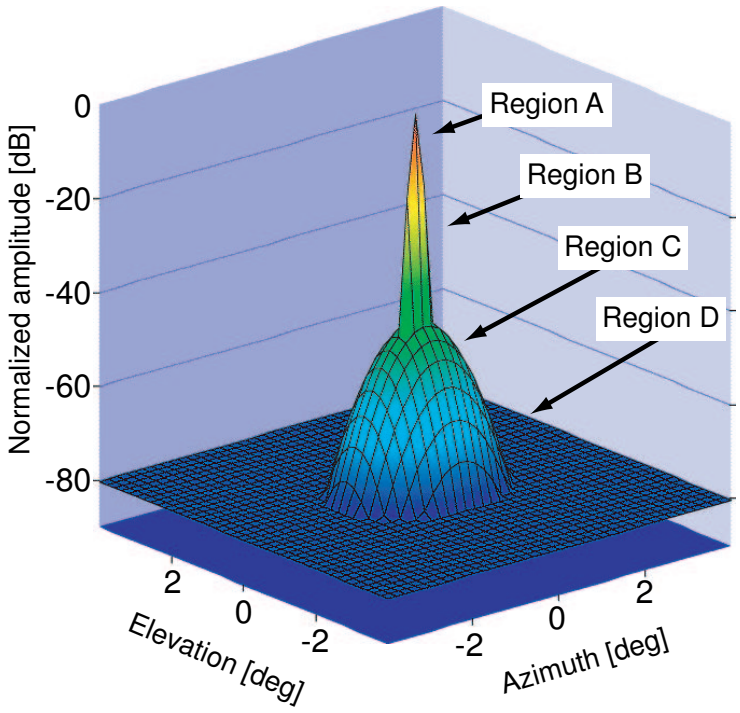

Figure 3.17 Approximate response pattern. Region A is an area to define the FOV beam efficiency. Region B represents the main beam area. The response pattern in region B is approximated by a gaussian function. Region C describes an error pattern area. The response pattern in region C is described by second order polynomials of azimuth and elevation angles in decibel values. Region D is a wide angle pattern area. Its response function is described by a constant.

Table 3.10 Response pattern model coefficients for several cases in FOV beam efficiency. Coefficients $a_0 \sim a_3$ and $b_1 \sim b_5$ are common for all cases. Coefficients b_0 and c_0 in each case are different.

(a) Common coefficients

a_0	a_1	a_2	a_3	
-9.2377 $\times 10^{-5}$	1.0026	7.1774 $\times 10^{-2}$	3.4227 $\times 10^{-2}$	
b_1	b_2	b_3	b_4	b_5
0.92124	-0.23690	-11.084	-0.45984	-18.485

(b) Different coefficients

FOV beam efficiency	96 %	90 %	85 %	80 %
b_0	-44.210	-29.042	-26.021	-24.133
c_0	-80.242	-79.963	-79.535	-79.254

is described by second order polynomials of azimuth and elevation angles as

$$P_{\text{error}}(Az, El) = b_0 + b_1 \times Az + b_2 \times El + b_3 \times Az^2 + b_4 \times Az \times El + b_5 \times El^2 \text{ [dB]}. \quad (3.3)$$

Region D is a wide angle pattern area. Its response function (P_{wide}) is described by a constant as following:

$$P_{\text{wide}}(Az, El) = c_0(= \text{constant}) \text{ [dB]}. \quad (3.4)$$

Then, the response function is determined by a maximum value among the three functions as

$$P(Az, El) = \max[P_{\text{main}}(Az, El), P_{\text{error}}(Az, El), P_{\text{wide}}]. \quad (3.5)$$

The FOV efficiency for the ideal response pattern is 96.1 %. However, the real FOV efficiency may deteriorate due to several causes, such as thermal distortion and mechanical misalignment. It is considered that these factors cause a decrease of main beam gain and an increase of power level in the error pattern region. Following this assumption, the model coefficients are determined. We find model coefficients for four cases in FOV efficiency as shown in Table 3.10.

3.2.4.2 Effective Response Pattern for Atmospheric Limb Scanning

The antenna response pattern is usually expressed with a radiation characteristic in a certain cut plane such as Az=0. For the atmospheric limb scanning, however, an effective response pattern in the height direction is more important. Since the atmosphere is well stratified, the vertical response pattern $P_{vert}(El)$ is obtained from the following equation:

$$P_{vert}(El) = \int_{Az_-}^{Az_+} P(Az, El) \cos(El) d(Az), \quad (3.6)$$

where $P(Az, El)$, Az_+, and Az_- represent the antenna response function, and the azimuth boundary angles of the FOV. Based on the actual extent of the open window for the antenna, we assume that Az_+ and Az_- is +99° and -5°, respectively. As previously mentioned in 3.2.1.3, atmospheric emissions from six consecutive tangent point altitudes

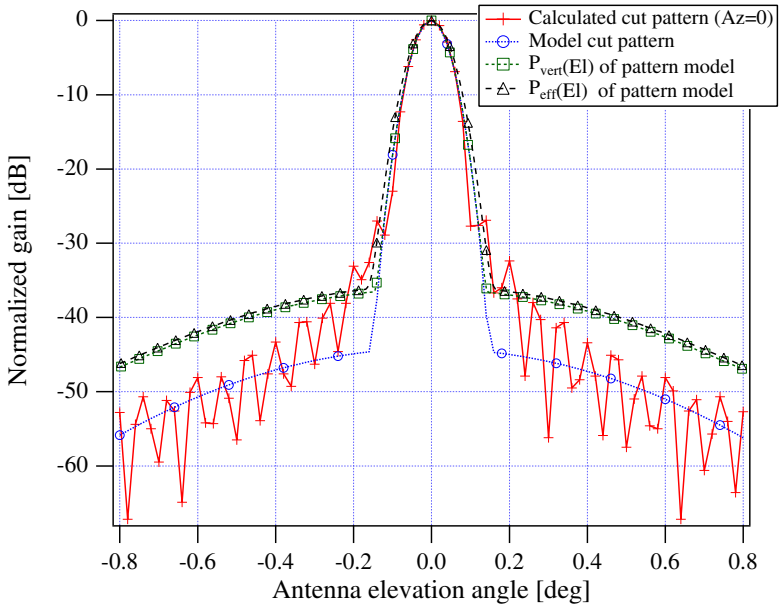

Figure 3.18 Effective antenna response pattern.

will be collected and integrated in each unit of the output data. Therefore, the effective response pattern $P_{eff}(El)$ is calculated by averaging $P_{vert}(El)$ for six consecutive altitudes as the following:

$$P_{eff}(El) = \frac{1}{6}\sum_{j=0}^{j=5} P_{vert}(El + (j - 2.5)\Delta El), \tag{3.7}$$

where ΔEl is a unit stepping angle of the SMILES antenna, 0.009375°, which is driven by the Antenna Drive Electronics (ADE).

Figure 3.18 shows the vertical and the effective antenna responses for the pattern model in comparison with cut-responses at $Az = 0$ for the designed pattern and the model pattern.

All patterns are normalized by each antenna gain. The result shows the sidelobe levels of the vertical and the effective antenna response pattern are approximately 9 dB higher than those of the cut response pattern. It means that SMILES has a higher sensitivity to the atmospheric emissions at adjacent altitudes than expected simply from the vertical cut response pattern.

The HPBW of the vertical response pattern is similar to that of the cut response pattern of the model. They are 0.080°. The effective beam size is 0.090° in HPBW, which is 12 % larger than that for the cut response pattern of the model.

3.2.4.3 Beam Efficiency

In the SMILES antenna specification, the FOV beam efficiency is defined by the ratio of the power radiated into an elliptical cone with a flare-angle of 2.5-time HPBW to the total power radiated by a feed horn. The feed horn adopted for SMILES is a so-called "back-to-back horn," which is placed at the interface point between the SMILES antenna and the Ambient Temperature Optics (AOPT). It is a circular corrugated waveguide with

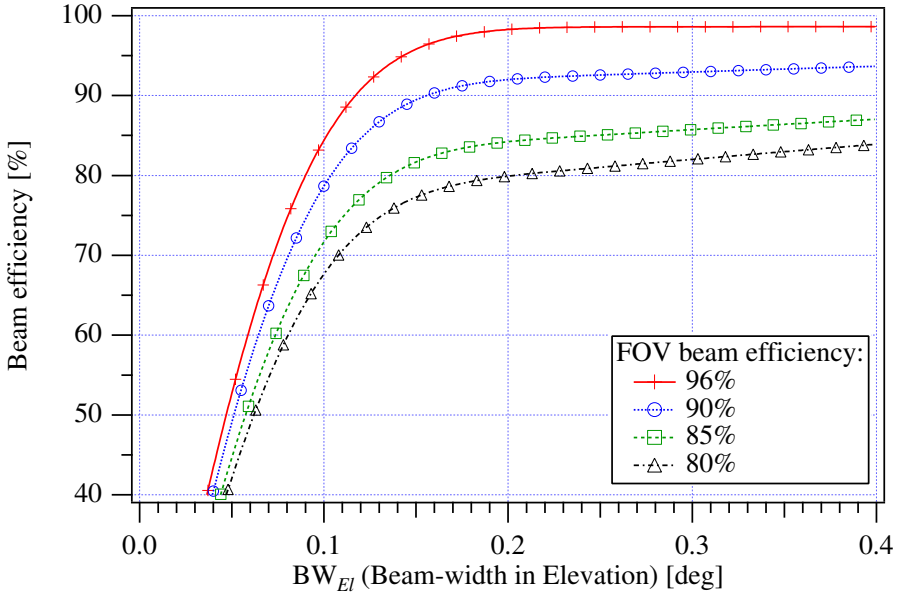

Figure 3.19 Beam efficiency.

a taper in one end, which will feed the antenna. This optical approach is adopted to make electro-magnetic shielding for the sensitive submillimeter receiver against high-level artificial electric fields anticipated on the ISS. To understand the relationship between the beam efficiency and a degradation of the beam quality, we have calculated a beam efficiency as a function of a beam width in the elevation angle, BW_{El}. Such function is defined by

$$\eta_{beam}(\mathrm{BW}_{El}) = \frac{\int_{-\mathrm{BW}_{El}/2}^{\mathrm{BW}_{El}/2} P_{vert}(El)d(El)}{P_{total}}, \tag{3.8}$$

where P_{total} is the total power and BW_{El} is the full extent of the elevation angle to define the beam efficiency.

The calculated results are shown in Figure 3.19. We have assumed that the FOV beam efficiencies are 96 %, 90 %, 85 %, and 80 %. A decrease in the FOV beam efficiency represents a decrease in the main beam power level and the increase in a error pattern power level. When the FOV beam efficiency is higher than 90 %, the beam efficiency will approximately saturate around the definition area of the FOV beam efficiency, which is the 2.5 times as wide as the HPBW_{El}.

We will discuss the effect of the FOV beam efficiency on the brightness temperature in detail in 3.3.5.

3.2.5 ISS Orbit and Attitude Variations

3.2.5.1 Orbit

The ISS is in a nearly circular orbit with an altitude of 350 – 460 km and an inclination of 51.6° to the equator. Major characteristics of the orbit are listed in Table 3.11 [*NASA*, 2000]. The orbit will decay due to atmospheric drag on the ISS, which is enlarged with its

low altitude and large cross section. The lower limit of the ISS altitude, for its existence in orbit, is taken as 278 km. The operational altitude must be kept higher than 350 km, where the orbital decay takes 180 days to reach the lower limit. Periodic boosting by using onboard thrusters will be carried out to maintain the ISS altitude within 350 – 460 km. The orbit control accuracy is specified as 305 m (3σ) in terms of the semi-major axis. The orbit determination accuracy is 305 m (3σ) for the semi-major axis, and 914 m (3σ) for the position vector. The ISS orbit prediction data will be found on the NASA website at http://spaceflight.nasa.gov/realdata/sightings/SSapplications/Post/JavaSSOP/orbit/ISS/SVPOST.html, and orbit determination data will be provided from the NORAD data website at http://celestrak.com/NORAD/elements/.

Table 3.11 Characteristics of the ISS Orbit

Parameters	Characteristics
Nominal Orbit	Altitude : 407 km Inclination : 51.6°
Range of Operational Altitude	350 km to 460 km
Orbit Control Accuracy	Semi-major axis : 305 m (3σ)
Orbit Determination Accuracy (Knowledge Accuracy)	Semi-major axis : 305 m (3σ) Position vector : 914 m (3σ)
Orbit Prediction Accuracy	TBD

Table 3.12 ISS Orbital Elements

Prediction Data			
Website	Coordinates	Description	Notes
NASA	M50 cartesian	position, velocity	M50 : Inertial mean of year 1950 frame of reference
	M50 keplerian	6 orbital elements	
	M50 cartesian	position, velocity	J2000 : Inertial mean of year 2000 frame of reference
	J2000 cartesian	position, velocity	
	Keplerian	TLE (5 orbital elements, mean mortion)	TLE : Two-lines elements
	Keplerian	AMSAT (5 orbital elements, mean mortion)	
Determination Data			
NORAD	Keplerian	NORAD TLE (5 orbital elements, mean mortion)	

3.2.5.2 Attitude Control

The ISS will fly in the so-called "Local Vertical Local Horizontal (LVLH)" attitude. This means that the ISS attitude is nominally fixed in a reference coordinate that is defined

by a local horizontal plane and a local vertical direction (nadir). Since the ISS attitude is affected by perturbation torque due to aerodynamic drag and gravity gradient, it is controlled by a set of onboard Control Moment Gyros (CMGs) to maintain the Torque Equilibrium Attitude (TEA). Major characteristics of the ISS attitude are shown in Table 3.13 [*NASA*, 2000; *Treder*, 1999]. Absolute tilt angles are allowed up to $\pm 15^\circ$ in roll and yaw, and $-20/+15^\circ$ in pitch. These angles depend on the mass characteristics of the whole ISS and atmospheric changes due to the solar activity. Its stability during a cycle period of orbit is specified to be within 3.5° per axis, and the rate of attitude change is within $\pm 0.002^\circ$/sec per axis. This attitude change rate is formally applied to the pressurized modules during microgravity operations. During a unit scan of the SMILES antenna, which lasts 53 seconds, the track of the scanning beam can deviate from an ideal straight ascending line by about the same size as its HPBW. We have to determine the real track with a help of the star tracker that is equipped in SMILES.

Table 3.13 Characteristics of the ISS Attitude (TEA:Torque Equilibrium Attitude)

Parameters	Characteristics
Nominal Attitude	LVLH attitude
Range of Operational Attitude	Roll, Yaw : $+15^\circ$ to -15° Pitch : $+15^\circ$ to -20°
Attitude Control Accuracy	$\pm 5^\circ$ per axis (compared with the commanded values)
	$\pm 3.5^\circ$ per axis (controlling to TEA)
Attitude Change Rate	Within $\pm$ 0.002°/sec per axis (during microgravity operations, in pressurized labs)
Attitude Estimation Accuracy	0.5° per axis (3σ) 0.01°/sec per axis (3σ)
(Knowledge Accuracy)	(at the NASA navigation base) 3.0° per axis (3σ) (at attached payload)
Attitude Prediction Accuracy	TBD
Continuous Period in the TEA	30 days

3.2.6 Tangent Height Calibration

3.2.6.1 Calibration Scheme

By comparing observed stellar images with an installed star catalog, the Star Tracker (STT) will calculate the orientation of the mechanical framework of the STT camera in the heliocentric inertial equatorial reference coordinate system (HCS) which is an inertial coordinate system with its origin located at the sun and its equatorial plane in the earth orbital plane. The STT on SMILES provides the output in the quaternion representation. It is a method to express a rigid-body rotation by means of the direction cosines (e_1, e_2, e_3) of an axis and a rotation (Φ) around the axis. Four parameters of the quaternion is

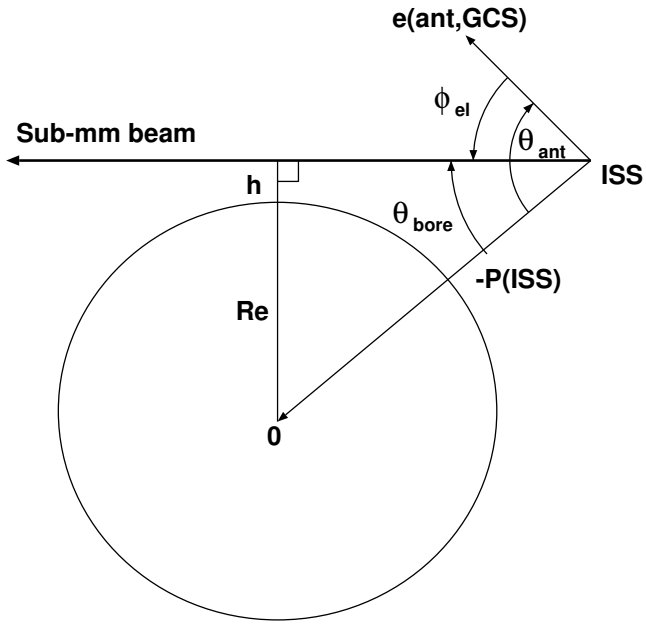

Figure 3.20 Geometrical definition of tangent-point altitude

defined as

$$q_1 \equiv e_1 \sin\frac{\Phi}{2}, \tag{3.9}$$

$$q_2 \equiv e_2 \sin\frac{\Phi}{2}, \tag{3.10}$$

$$q_3 \equiv e_3 \sin\frac{\Phi}{2}, \tag{3.11}$$

$$q_4 \equiv \cos\frac{\Phi}{2}. \tag{3.12}$$

With these four parameters, we can express any rigid-body rotation by the following matrix.

$$\boldsymbol{M}[\boldsymbol{q}] = \begin{bmatrix} q_1^2 - q_2^2 - q_3^2 + q_4^2 & 2(q_1q_2 + q_3q_4) & 2(q_1q_3 - q_2q_4) \\ 2(q_1q_2 - q_3q_4) & -q_1^2 + q_2^2 - q_3^2 + q_4^2 & 2(q_2q_3 + q_1q_4) \\ 2(q_1q_3 + q_2q_4) & 2(q_2q_3 - q_1q_4) & -q_1^2 - q_2^2 + q_3^2 + q_4^2 \end{bmatrix}. \tag{3.13}$$

If a unit vector in the STT-based coordinate is represented by $\boldsymbol{e}(stt)$, the direction of the antenna mounting basis (a reference direction corresponding to the antenna elevation angle of 0°) that is evaluated in the geodetic coordinate system (GCS), which is an earth-based coordinate with its origin at the earth center and its equatorial plane in the earth equator, $\boldsymbol{e}(ant, GCS)$, is calculated by

$$\boldsymbol{e}(ant, GCS) = \boldsymbol{M_2} \cdot \boldsymbol{M_1} \cdot \boldsymbol{K}(ant, stt) \cdot \boldsymbol{e}(stt), \tag{3.14}$$

where $\boldsymbol{M_1}$ and $\boldsymbol{M_2}$ are coordinate transformation matrices to express the conversion from the STT-based coordinate to the heliocentric inertial equatorial coordinate system (HCS), and that from the HCS to the GCS, respectively. The matrix elements of $\boldsymbol{M_1}$ are expressed with the quaternion components of the STT outputs. Matrix $\boldsymbol{K}(ant, stt)$ denotes a vector

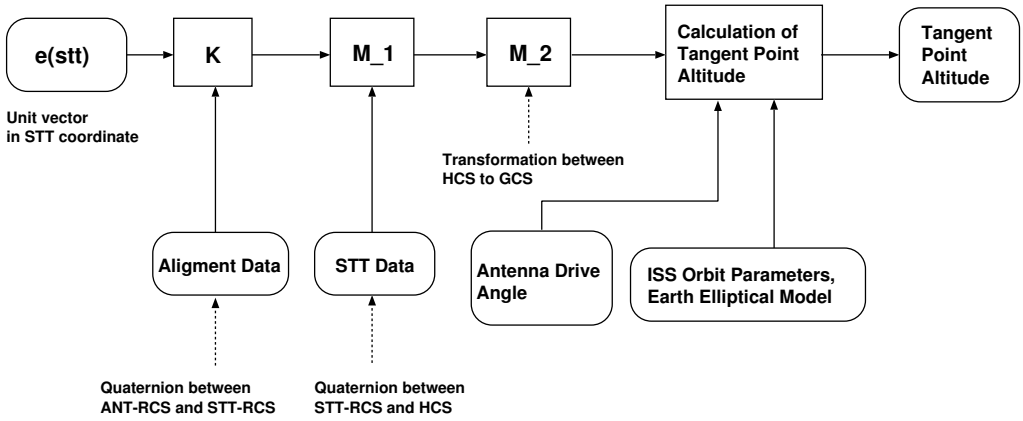

Figure 3.21 Flow chart of STT data analysis

rotation from the unit vector of the STT-based coordinate to the axis of the antenna-mounting basis. Matrix $\boldsymbol{M_2}$ includes transformation in time system. A difference between the UT1 and UTC should be taken into account (UT1 represents the rotation of the earth while UTC are determined on the base of atomic time).

The tangent-point altitude for the limb-sounding observations is derived from $\boldsymbol{e}(ant, GCS)$ and information such as the ISS position in orbit, scanning angle of the antenna, and surface model of the Earth. The STT is mechanically fixed to the antenna-mounting basis, while the main reflector of the antenna will rotate around the elevation angle (ϕ_{el}). If the ISS position is determined with a position vector $\boldsymbol{P}(ISS)$ in the GCS, the angle between the line-of-sight of the antenna (mechanical axis) and $\boldsymbol{P}(ISS)$ is calculated as

$$\theta_{bore} = \arccos\left[\frac{-\boldsymbol{P}(ISS)\boldsymbol{e}(ant, GCS)}{\mid \boldsymbol{P}(ISS) \mid}\right] - \phi_{el}. \tag{3.15}$$

The tangent-point altitude is given by

$$h = \mid \boldsymbol{P}(ISS) \mid \sin\theta_{bore} - R_e, \tag{3.16}$$

where R_e represent the Earth radius at the tangent point.

3.2.6.2 Calibration Accuracy

Several factors that affect the accuracy of tangent point height are listed in Table 3.14. They include errors both in the attitudes of the SMILES antenna and in the ISS orbital altitude. Among the attitudinal errors are the squint of the submillimeter beam from the mechanical axis of the antenna reflector, offset angle in the driving mechanism of the antenna, thermal bending of the antenna structure with respect to the STT, alignment errors between the antenna and STT, measurement errors in the STT, and errors due to imperfect time synchronization between the ISS and STT. On the other hand, errors in the ISS orbit determination will affect the knowledge of tangent point height. Expected error values for those factors are given in two columns for bias and random errors. Bias error means its effect is applied in common to all of the data acquired in a unit scan of the antenna (in 53 sec). The relative altitude distance between any two points is not affected by the bias errors. But random error occurs independently for each point. While

the current estimation of those error values are very tentative, we expect that the beam squint will be the largest factor in bias errors. It should be calibrated in orbit by means of observing a reference object such as the moon. The overall altitudinal error without the beam squint is estimated about 0.76 km in bias error, and 0.34 km in random error (both in 1σ).

Table 3.14 Residual Errors in the tangent height after calibration with the STT data

Error Factors	Bias Error@1σ		Random error@1σ	
Attitudinal Errors:				
Sub-mm beam offset from the REF axis	0.13°	5.02 km	–	–
Mechanical driving errors of REF	0.007°	0.27 km	0.007°	0.27 km
Thermal bending of REF against STT	0.003°	0.12 km	–	–
Mechanical alignment of REF against STT	0.007°	0.27 km	–	–
STT measurement errors	0.007°	0.27 km	0.0015°	0.06 km
Time synchronization errors	0.20 sec	0.50 km	0.07 sec	0.18 km
Altitudinal Error:				
Determination errors of the ISS position	–	0.3 km	–	0.1 km
Overall(rss) with the beam offset		5.07 km		0.34 km
Overall(rss) without the beam offset		0.76 km		0.34 km

REF means the main and sub reflectors of the antenna. STT is the Star Tracker. Altitudinal sensitivity to the attitude error is 38.6 km/deg, and that to the error in time is 2.52 km/sec for the nominal orbital height of 400 km.

3.3 Spectral Regions and Sensitivity

3.3.1 Observation Frequency Bands

Three observation frequency bands have been selected in line with the SMILES scientific objectives toward chlorine-related processes in the stratosphere. Most important molecular transitions included in these bands are 649.45 GHz (ClO), 625.92 GHz ($H^{35}Cl$) and 624.98 GHz ($H^{37}Cl$), as well as 625.37 GHz and others for O_3. This selection is a result of optimization between scientific targets and instrumental restrictions, such as the number of SIS mixers and down-converters. The first intermediate frequency (IF) is determined to avoid potential interference by high-level electromagnetic fields in the ISS environments. A spectral range around 650 GHz and the other around 625 GHz are simultaneously observed in the upper sideband (USB) and lower sideband (LSB), respectively, of the submillimeter mixing with a single local oscillator (LO) at 637.32 GHz. In Figures 3.22-3.24, expected emission profiles are calculated based on a standard model of the atmosphere (Rutherford Appleton Laboratory). The brightness temperature and line-width of the atmospheric emissions are widely varied, depending on the tangent altitude of the observing line-of-sight. Frequency coverage is 624.32 - 625.52 GHz in Band-A, 625.12 – 626.32 GHz in Band-B, and 649.12 – 650.32 GHz in Band-C. As SMILES has only two units of spectrometers, only two among these three bands are observed at a time. Nevertheless, Band-A and Band-B are partially overlapped to keep observations of O_3 at 625.37 GHz being conducted in any cases. HCl lines are observed in both Band-A and Band-B, while they are attributed to different isotopes of chlorine. The natural abundance of ^{35}Cl and ^{37}Cl is 75.78 percents and 24.22 percents respectively. ClO is observed only in Band-C. There are two ^{81}BrO

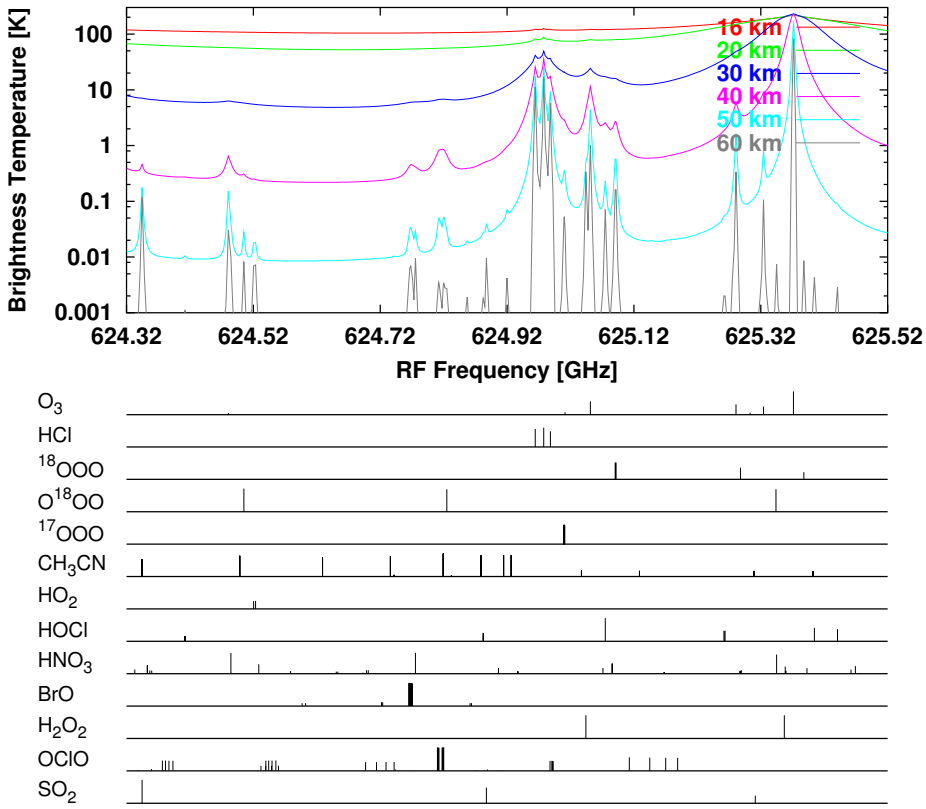

Figure 3.22 Atmospheric emission profiles expected for Band-A.

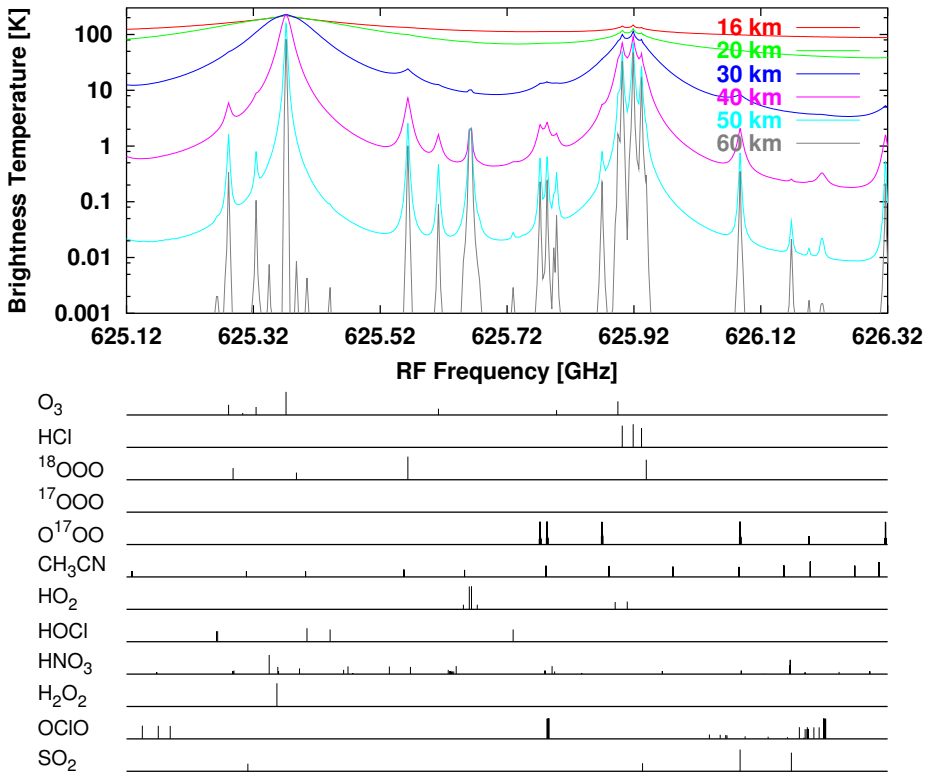

Figure 3.23 Atmospheric emission profiles expected for Band-B.

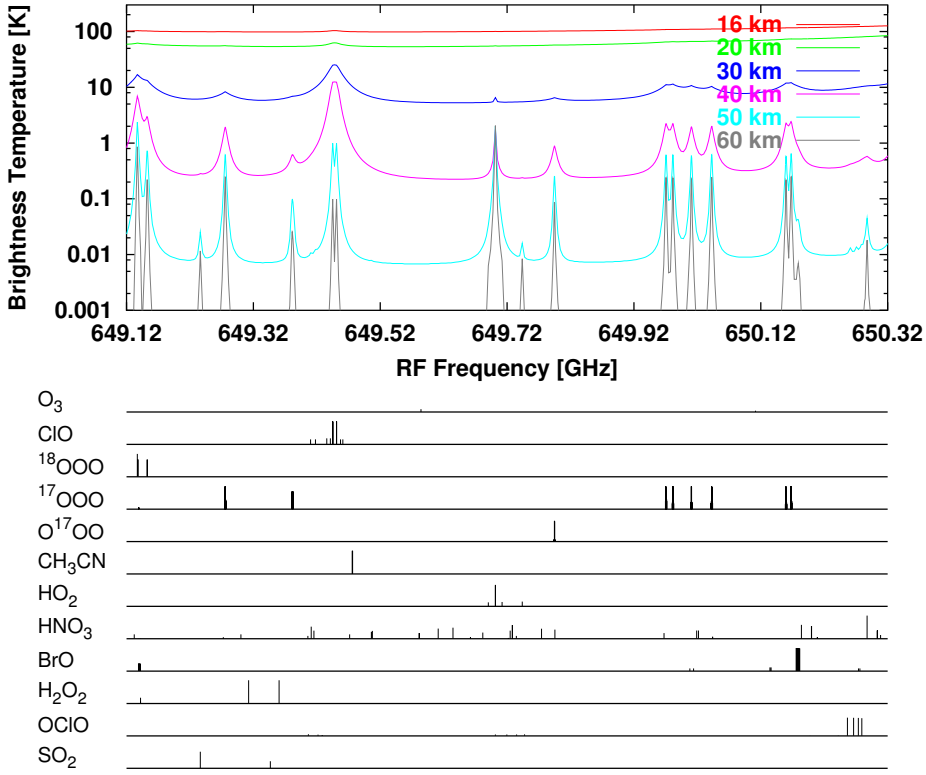

Figure 3.24 Atmospheric emission profiles expected for Band-C.

lines, at 624.77 GHz and 650.18 GHz, included in Band-A and Band-C.

3.3.2 Frequency Down-conversion

3.3.2.1 Intermediate Frequency System

The three submillimeter-wave bands are converted to the first IF by two SIS mixers operated at 4.5 K in a cryostat [*Fujii et al.*, 2000; *Inatani et al.*, 1997]. By means of a quasi-optical single-sideband (SSB) filter, the USB and LSB emissions are separately converted to the first IF, which is 11.8 – 13.0 GHz for the USB and 11.0 – 13.0 GHz for the LSB. Band-A and Band-B are two different portions inside the LSB, while Band-C is in the USB. These are further down-converted to the second IF in 1.55 – 2.75 GHz, and spectral features in each band are analyzed by the Acousto-optic Spectrometer (AOS).

When a microwave mixer is sensitive to both its USB and LSB, the sideband of interest is called a "signal band," and the other undesirable sideband is an "image band." Even with an SSB filter, its performance to reject an image band is not perfect. This situation makes it important to know how the image band is superimposed on the signal band. Figure 3.25 illustrates how the three submillimeter-wave observation bands are converted down to the second IF.

3.3.2.2 Sideband Separation

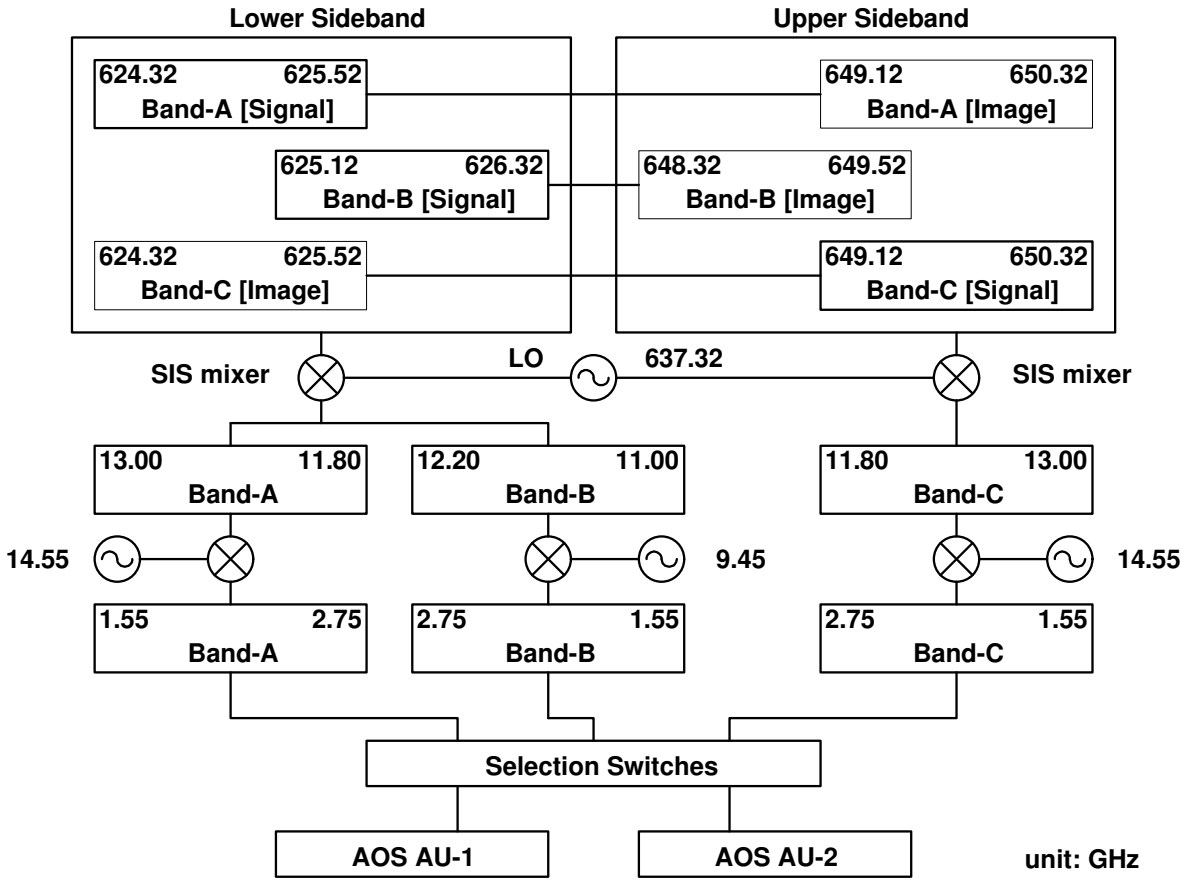

Figure 3.25 Frequency conversion in SMILES: Both signal and image bands are converted to the first IF, while the image is suppressed by an SSB filter. The frequency conversion to the second IF is made completely in a single sideband mode.

Figure 3.26 illustrates the schematic configuration of SSB filtering and local injection in the receiver optics of SMILES. To separate the two sidebands, SMILES is equipped with a quasi-optical SSB filter in its submillimeter optics. The SSB filter, which is a modified Martin-Puplett interferometer [*Inatani et al.*, 1999] newly proposed for SMILES, has the ability to reject the image band by 20 dB or more in the SMILES observation bands. This proposed SSB filter is composed of a pair of frequency-selective polarizers (FSP1 and FSP2) each of which consists of a free-standing wire-grid backed by a flat mirror, and is intended to achieve a function as a dual-beam interferometer equivalent to that of the conventional type Martin-Puplett interferometer (MPI) [*Martin*, 1982].

The functional blockdiagram of the sideband separation in the SMILES submillimeter-wave optics is shown in Figure 3.27. The SIS mixer-1 is well coupled to the antenna (ANT) in the USB, but is not in the LSB. In the LSB, it is coupled to the Cold-sky Terminator (CST), which is a reference port terminated to the 2.7-K cosmic microwave background. Since the CST is free from the atmospheric emissions, this method allows the SIS mixer-1 to selectively down-convert the USB atmospheric emissions into the first IF. In the same way, the SIS mixer-2 down-converts the LSB atmospheric emissions into the first IF. In addition to sideband separation, the SSB filter coupled with the wire-grids RG1 and LG1 has a function of injecting the local signal from the submillimeter-wave local

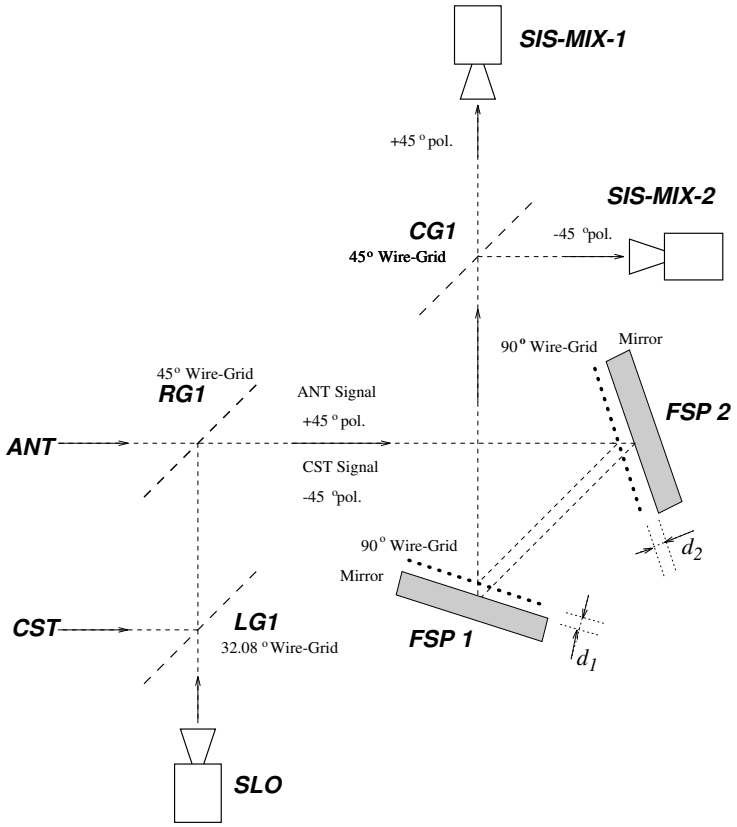

Figure 3.26 Schematic configuration of SSB filtering and local injection in the SMILES receiver optics

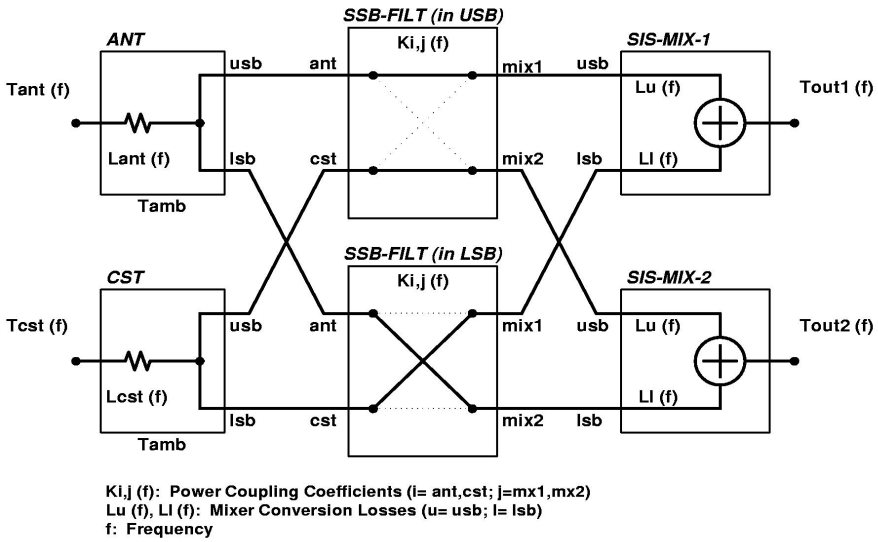

Figure 3.27 The function of the SSB filter in detail. The antenna port is coupled with the mixer-1 in the USB, but with the mixer-2 in the LSB. CST stands for the Cold-sky Terminator, which is free from the atmospheric emissions. Solid lines mean an efficient coupling, and dotted lines a suppressed coupling.

oscillator (SLO) to both LSB (SIS-MIX-1) and USB (SIS-MIX-2) mixers for frequency down-conversion.

The sideband separation characteristics of the modified Martin-Puplett interferometer are determined by the grid-mirror spacings, d_1 and d_2, of two FSPs. In the design of the SMILES submillimeter-wave opticas, a combination of the spacings, $d_1 = 1.545$ mm and $d_2 = 1.572$ mm, is adopted as a reasonable choise by which we can achieve image rejection better than 15 dB both for LSB and USB of SMILES observation bands while keeping the difference in local-signal power couplings to USB and LSB mixers less than 0.5 dB. The pass-band transmission and image rejection characteristics calculated around the SMILES obeservation bands by an exact theory for the two FSP combination are shown by red symbols in Fig. 3.28. Although the exact theoretical calculations are rather involved, the transmission and rejection characteristics around the SMILES observation bands are found to be well approximated by simple functions describing power coupling coefficients for the SIS mixer-i to the ANT port, $K_{i,a}$, and to the CST port, $K_{i,c}$, given by

$$K_{i,j}(f) = \frac{1 + \alpha^2 + 2\alpha \cos(\frac{m\pi f}{f_0})}{4} \qquad (i = 1 \text{ or } 2,\ j = a \text{ or } c). \tag{3.17}$$

A nonlinear least-squares fitting gave an exellent fit of (3.17) to the exact theoretical calculation as shown in Fig. 3.28 with the values of parameters, m, f_0 and α, listed in the

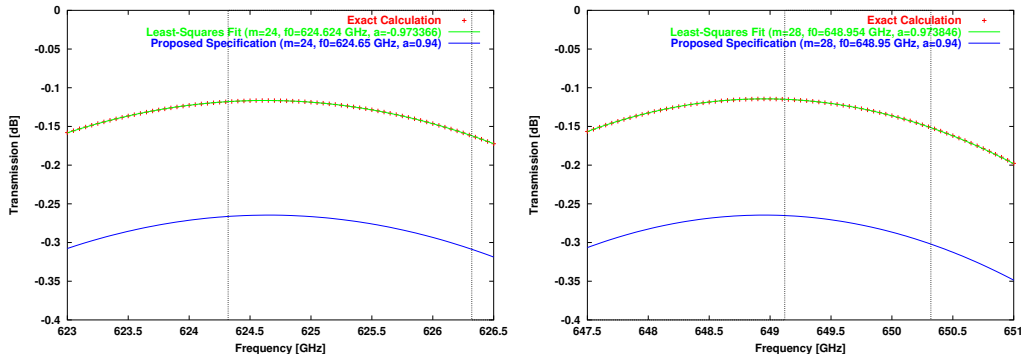

(a) Transmission Characteristics in LSB. (b) Transmission characteristics in USB.

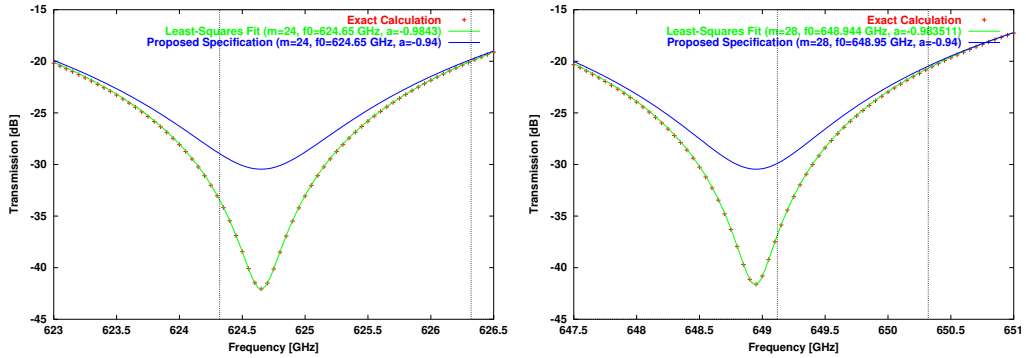

(c) Image rejection characteristics in LSB. (d) Image rejection characteristics in USB.

Figure 3.28 Coupling coefficient K_{ij} for signal transmission and image rejection of the SSB filter designed for SMILES. +: Exact theretical calculation for SSB filter; green curves: least-squares fit to the exact calculation; blue curves: simplified model for SSB characteristics of SMILES optics.

Table 3.15 Model parameters m, α, f_0 of power coupling coefficients K_{ij} for least-squares-fit model of SSB filter and simplified model for SMILES optics

			Least-Squares Fit			Proposed Specification		
Band		$K_{i,j}$	m	f_0	α	m	f_0	α
LSB	Transmission	$K_{1,a}, K_{2,c}$	24	624.624 GHz	0.973366	24	624.65 GHz	0.94
	Rejection	$K_{2,a}, K_{1,c}$	24	624.65 GHz	−0.9843	24	624.65 GHz	−0.94
USB	Transmission	$K_{2,a}, K_{1,c}$	28	648.954 GHz	0.973846	28	648.95 GHz	0.94
	Rejection	$K_{1,a}, K_{2,c}$	28	648.944 GHz	−0.983511	28	648.95 GHz	−0.94

columns labeled as *Least-Squares Fit*. By considering imperfectness of optical components not only in the SSB filter but also in whole optics, we propose to use a more conservative model given by (3.17) with the values of parameters, m, f_0 and α, listed in the columns labeled as *Proposed Specification* in Table 3.15. The power coupling coefficients given by this *Proposed Specification* is also shown in Fig. 3.28

With this *Simple Model*, the effects of the image band on the atmospheric observations are calculated in Figures 3.29 – 3.30. The image contribution suppressed by the SSB filter is superimposed on the signal spectra in the first IF. More precisely, we have to take account of the difference in the SIS mixer conversion losses for the USB and LSB, which could be up to 2 dB depending on particular device of the SIS mixer. But this effect is not included in Figures 3.29 – 3.31.

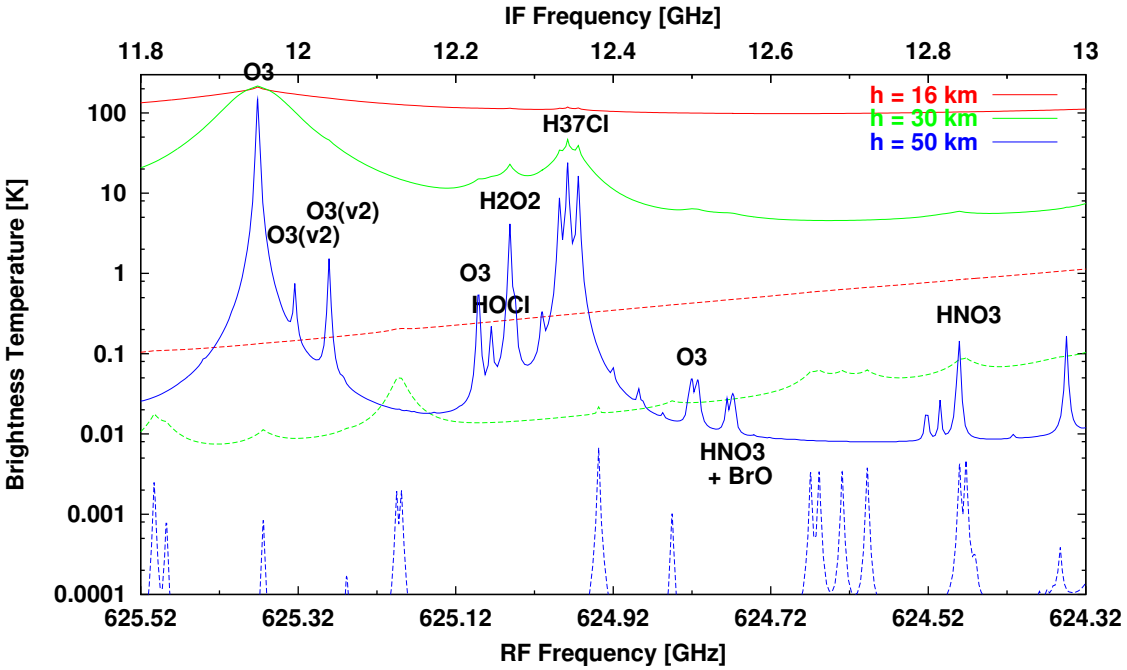

Figure 3.29 The effect of the image contributions in Band-A. Solid curves denote the signal intensities and dashed curves the image contributions.

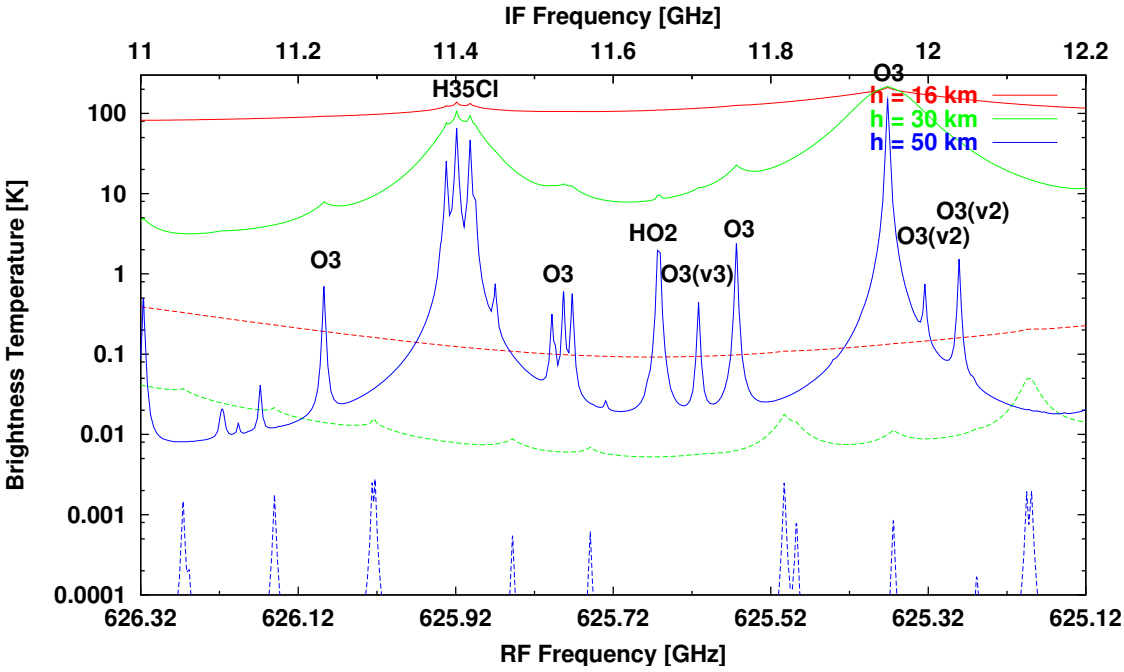

Figure 3.30 The effect of the image contributions in Band-B.

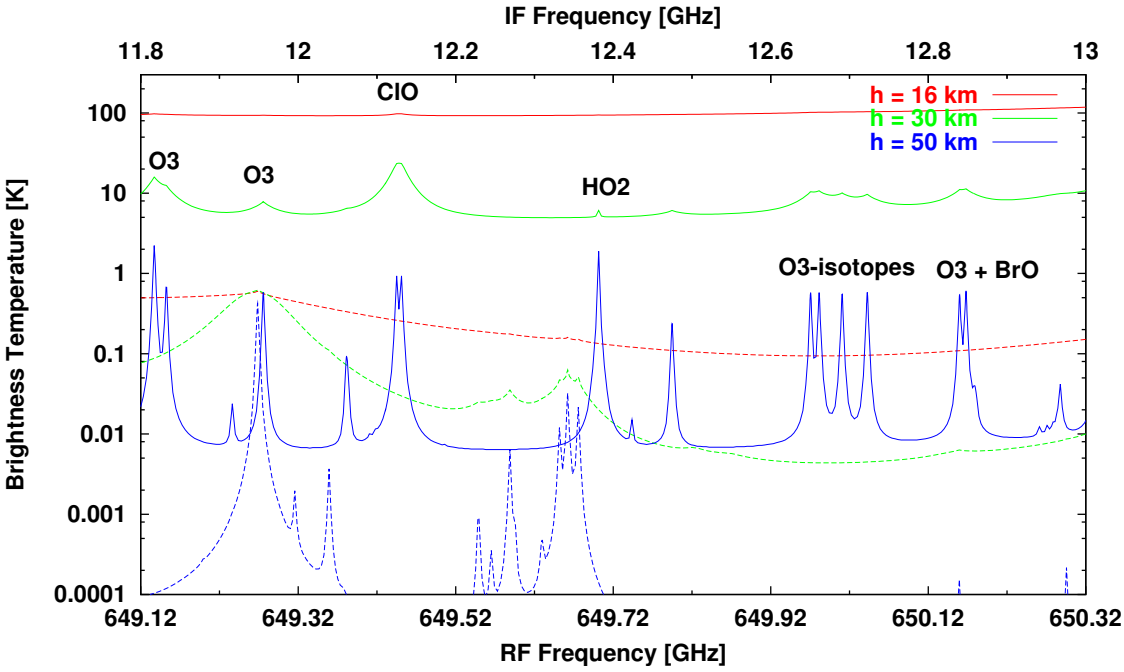

Figure 3.31 The effect of the image contributions in Band-C.

3.3.3 Acousto-optic Spectrometer

3.3.3.1 Frequency Characteristics

Two acousto-optic spectrometers (AOS) give us a powerful means of obtaining spectral images of various chemical species in a required range of altitudes, while constituting the system with a single type of spectrometer (see Figure 3.32). Each AOS has 1500 spectral channels to cover the bandwidth of 1200 MHz. Two units of AOS can be combined by selecting a mode in the IF switching network, which enables us to view a limb spectrum with a 2000-MHz bandwidth over 3000 frequency channels. Channel separation is typically 0.8 MHz, but the channel number is not always linearly related with its corresponding frequency. In addition, the relation can be influenced by the change of the environmental temperature. Some calibration process is needed on board, which is described in the remaining.

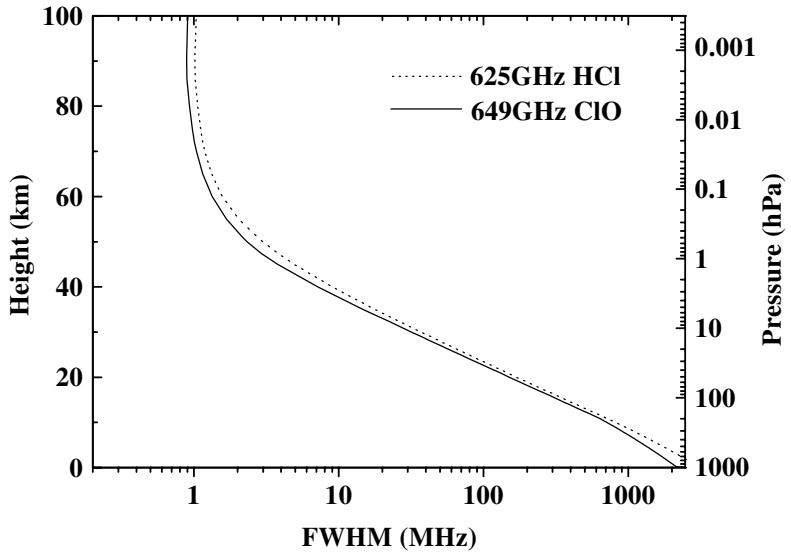

Figure 3.32 Spectral line-width versus atmospheric height with respect to two important lines of the SMILES mission.

Spectrometer's response function is obtained with the input of a carrier signal, the typical shape of which is depicted in Figure 3.33. Any input spectra to the AOS are convoluted with this kind of frequency response function, the full-width at half-maximum (FWHM) of which is often called as "resolution bandwidth" of the AOS. The FWHM for the AOS on SMILES will be 1.4 MHz or less. With this frequency response function, we can estimate the influence of some strong emissions at neighbor frequencies on the emission profile of interest.

On the other hand, when we deal with noise characteristic of the AOS, we should use the noise bandwidth, which represents the width of such an equivalent boxcar filter that gives the same fluctuations on the output spectra. The noise bandwidth for the AOS on SMILES is derived to be 2.5 MHz. With this value, we can estimate the standard deviation of the spectral fluctuations on the AOS output data. Each output spectrum is obtained in every 500 ms. If the system noise temperature is 500 K, the standard deviation for the

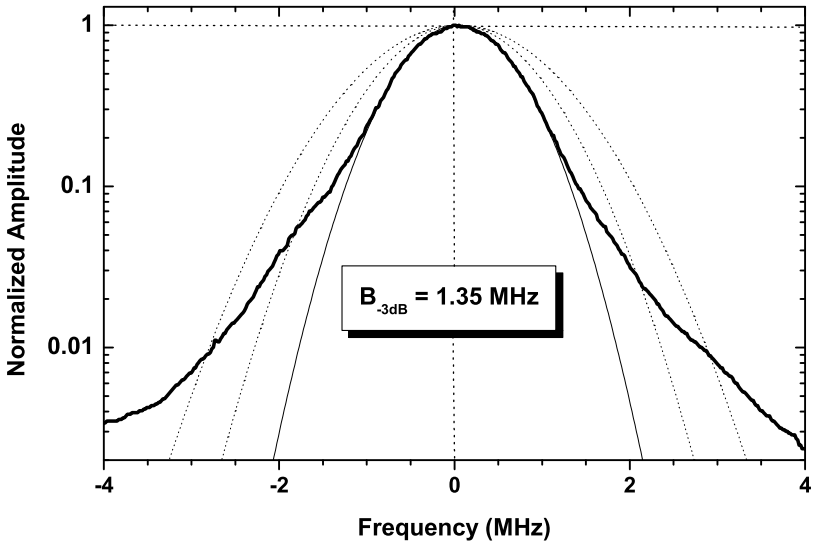

Figure 3.33 Frequency response function of the SMILES/AOS. The typical resolution bandwidth is 1.35 MHz.

snap shot spectrum will be approximately 0.5 K.

3.3.3.2 Frequency Calibration

Frequency calibration of the spectrometer will be accomplished by using a frequency reference with the absolute accuracy of about 10 kHz over the whole mission life. It is installed in the IFA section, generating a series of carrier signals with an interval of 100 MHz. The output of this comb generator will be injected to the AOS once in every scan of the antenna (53 seconds). Peak positions of each picket are derived against channel numbers, and the relation between frequency and channel number will be established by a polynomial fitting. Residuals of such fitting will be typically less than 30 kHz as shown in the Figure 3.34, which gives the error in frequency of the AOS spectra.

3.3.3.3 Noise Dynamic Range

Radio signal is converted to optical one in the AOS, and it is detected by a CCD array. The read-out voltages, or the number of collected charges in each cell of the CCD array, should be proportional to the input RF power levels, but they are usually modified by several additional factors in reality. The variance of the original RF noise at CCD is expressed by the following well-known expression:

$$N_{RF}^2 = \frac{Q^2}{B \cdot t}, \tag{3.18}$$

where Q,B, and t represent the number of collected charges at CCD, noise band-width, and the integration time for collecting charges, respectively. Potential contributors to

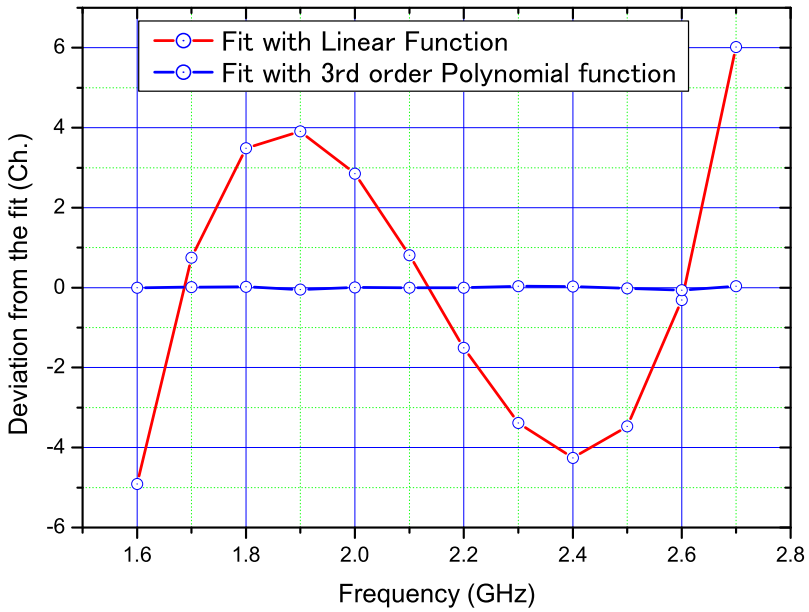

Figure 3.34 Residuals from the frequency fit with comb generator. 1 Ch. corresponds to approximately 0.8 MHz.

additional noise are photon shot noise, CCD dark noise, quantization noise, and detection circuit noise:

$$N_{add}^2 = N_{photon}^2 + N_{CCD}^2 + N_{AD}^2 + N_{Detection-circuit}^2. \tag{3.19}$$

The read-out noise of the AOS is the sum of the RF noise and the additional ones:

$$N_{read-out}^2 = N_{RF}^2 + N_{add}^2. \tag{3.20}$$

The relative weight of the additional noise will increase as the RF power decreases. So if a criterion is settled so that the noise variance ratio $N_{read-out}^2/N_{RF}^2$ to be less than 1.21, then we can define a range of RF power levels, for which the additional noise is less than 10%. We call this the "noise dynamic range" of the AOS. As far as the observed spectra lie within the noise dynamic range, the increase of the system noise due to the AOS can be negligible.

Alternatively, we can calculate an increase of noise at a given signal level. Its coefficient is a function of the signal level, and expressed as $f(D)$, where $D = Q_{sat}/Q$, and

$$T_{sys}^{eff} = T_{sys}^{org} \cdot f(D), \tag{3.21}$$

$f(D)$ can be calculated with the AOS instrumental parameters:

$$f(D) = \sqrt{1 + \frac{B \cdot t}{Q_{sat}} \cdot D + B \cdot t \left(\frac{q_0^2 + q_{eff}^2}{Q_{sat}^2} + \frac{1}{2^{2n} \cdot 12} \right) \cdot D^2}, \tag{3.22}$$

where, q_0, Q_{sat}, n, and q_{eff} are dark current noise, amount of the saturation charge, quantization bit of the A/D converter, and equivalent amount of charge of the detection

circuit noise, respectively. A typical behavior of $f(D)$ is depicted in Figure 3.35. In SMILES/AOS, the noise dynamic range of 9 dB is foreseen for a criterion of additional noise of 10%.

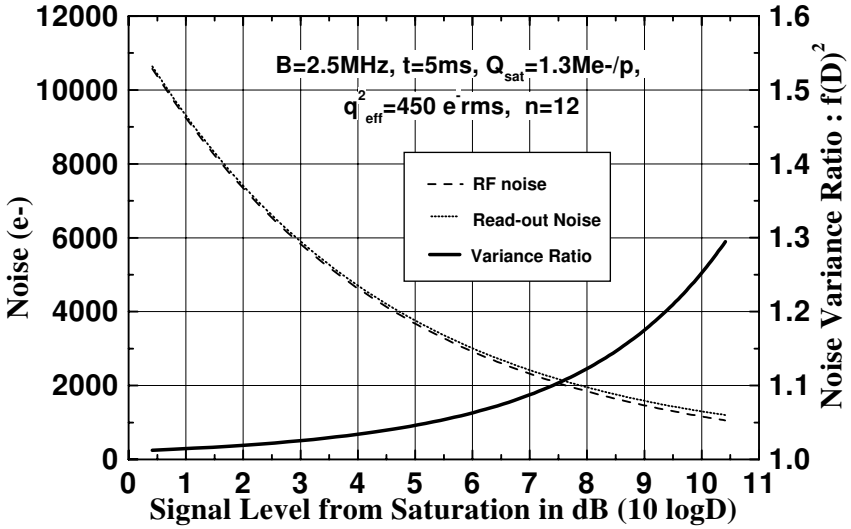

Figure 3.35 RF noise, read-out noise and the variance ratio of them

3.3.3.4 Differential Non-Linearity

Another concern with the AOS in obtaining the limb spectrum is "differential non-linearity (DNL)" of the analog to digital converter, which was first claimed by R. Schieder of the University of Cologne. The DNL is irregularities in the "monotonic character" of the conversion from input analog voltages to digitized values. Noise due to this effect is non-statistical, because it is reproducible if we repeat measurements under the same conditions. It is troublesome that this effect is never visible as far as the signal and the reference are of the same power level, which is usually the case when a long-term integration test is performed in a laboratory. The Allan variance test also can never be an indicator of this effect. For atmospheric observations, however, the input power levels are largely separated between the signal and the reference. This makes it indispensable for us to pay an extra attention to this issue. It is difficult to predict the exact effect of the DNL for the SMILES/AOS, because the characteristics of A/D converters are varied among individual products. Nevertheless, we can simulate the atmospheric observation based on the characteristics of the A/D converter of the same type as planned to be used for the SMILES/AOS.

Figure 3.36 shows the effect of the differential non-linearity on the observed spectra. ΔT denotes the difference between the digitized and the analog values of the brightness temperature. We see that a specific undulation of the spectrum appears, and it remains unchanged even after 60 times of accumulation of the spectrum, which corresponds to a one-day average for a zonal map with a latitudinal interval of 5°. The magnitude of the undulation depends heavily on the temperature of the limb spectrum. If the brightness temperature of the limb spectrum is not so different from the reference sky, this effect is

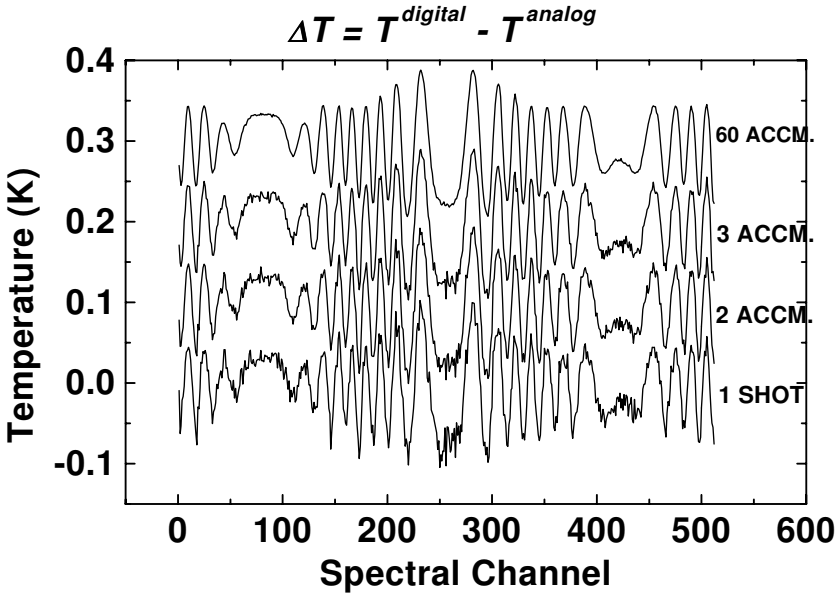

Figure 3.36 Simulated effects of the differential non-linearity on the spectrum for 1 shot, and for 2, 3, and 60 accumulations. The latter three spectra are shifted upward by 0.1, 0.2 and 0.3 K, respectively. The difference in brightness temperature between the limb atmosphere and the reference sky is taken as 20 K, and no gain variation is assumed in each integration period.

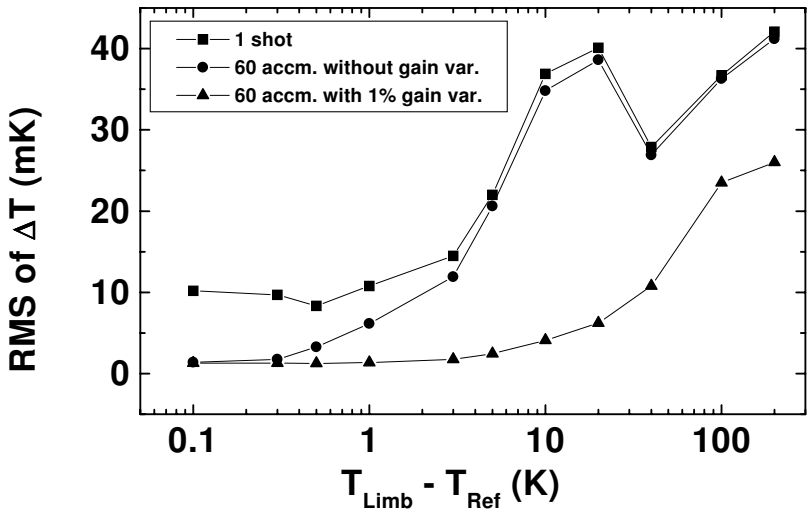

Figure 3.37 Dependence of the DNL effect on the difference of brightness temperature between the limb atmosphere and the reference sky.

much suppressed. On the contrary, the DNL effect cannot be ignored for low altitudes (high brightness temperatures).

Though the DNL is troublesome in measuring the atmospheric spectra, it is found that a small variation of the system gain has a possibility to smooth out this effect efficiently. Figure 3.37 shows the DNL effect against the difference in the input power levels between the two spectra. The lowest plot in the figure depicts an improvement of the sensitivity by including a "random" gain variation of 1% over 60 observational opportunities. This phenomenon will be rationalized by the shift of the "operational point" due to the gain variation. This plot tells us that if a gain variation occurs randomly, the DNL effect will be removed by accumulation. In the real observational conditions, the result will be between the two plots in the figure.

3.3.4 Sensitivity

3.3.4.1 Radiometric Noise

The sensitivity of SMILES to detect molecular emissions is mainly determined by the system noise temperature, T_{sys}, which is expressed by the following equation for the upper sideband observation (see Figure 3.27):

$$\begin{aligned} T^u_{sys} &= \begin{pmatrix} 1 & A^l & C^u & C^l \end{pmatrix} \cdot \begin{pmatrix} T^u_{ant} + T_{amb} \cdot (L_{ant} - 1) \\ T^l_{ant} + T_{amb} \cdot (L_{ant} - 1) \\ T^u_{cst} + T_{amb} \cdot (L_{cst} - 1) \\ T^l_{cst} + T_{amb} \cdot (L_{cst} - 1) \end{pmatrix} \\ &+ T^{dsb}_{rx} \cdot \left(1 + \frac{L_u}{L_l}\right) \cdot \frac{L_{ant}}{K^u_{ant}}, \end{aligned} \tag{3.23}$$

$$A^l = \frac{K^l_{ant}}{K^u_{ant}} \cdot \frac{L_u}{L_l}, \quad C^u = \frac{K^u_{cst}}{K^u_{ant}} \cdot \frac{L_{ant}}{L_{cst}}, \quad C^l = \frac{K^l_{cst}}{K^u_{ant}} \cdot \frac{L_{ant}}{L_{cst}} \cdot \frac{L_u}{L_l}. \tag{3.24}$$

Here T_{ant} and T_{cst} are input power levels to the Submillimeter Antenna (ANT) and Cold-sky Terminator (CST), expressed in brightness temperatures. Superscripts u and l indicate that the quantity is evaluated in the USB and LSB, respectively. T_{amb} is the brightness temperature for a black-body at the ambient temperature. L_{ant} and L_{cst} are propagation losses in the ANT and CST. T^{dsb}_{rx} is the receiver noise temperature evaluated in the double sideband (DSB) mode. This is the most dominant factor of the system noise temperature, and it is mainly determined by the performance of the submillimeter mixer inside the receiver. SMILES adopts cryogenically-cooled superconductive SIS mixers, instead of the conventional semiconductor diode mixers, to drastically reduce the value of T^{dsb}_{rx}. L_u and L_l are mixer conversion losses in the USB and LSB. These values are also much reduced in SIS mixers compared with the diode mixers. K_{ant} and K_{cst} are the mixer's power coupling coefficients with the ANT and CST, which are determined by the performance of the quasi-optical SSB filter. With this T^u_{sys}, the receiver output power corresponding to an input signal ΔT to the antenna is expressed as

$$T^u_{out} = (\Delta T + T^u_{sys}) \cdot \frac{K^u_{ant} G_{if}}{L_{ant} L_u}. \tag{3.25}$$

The minimum detectable temperature (1-sigma) is evaluated by the radiometer equation,

$$T_{rms} = \frac{T_{sys}}{\sqrt{B \cdot \tau}}, \tag{3.26}$$

where B is a detection noise bandwidth and τ is an integration time. T_{sys} of SMILES is about 500 K, for cases where the noise contribution from the atmosphere itself can be neglected. With B=2.5 MHz, τ=0.47 sec, the above equation gives a value of 0.46 K (rms).

3.3.4.2 Gain Stability

The second factor that can affect sensitivity is gain variation of amplifiers in the receiver system. Since the receiver gain is calibrated in every 53 seconds, our concern is variations in this short time scale. They will occur due to changes in the physical temperature of amplifiers. They can be separated into two parts: (1) a change in the relative frequency characteristics of the gain (we call this "gain fluctuation"in this chapter), and (2) a parallel shift of gain levels while the relative frequency characteristics are kept unchanged. The former will affect the sensitivity to spectrum, but the latter will be related only to the absolute calibration accuracy of brightness temperatures. The former amplitude is considered to be much smaller than the latter one. In order that the former fluctuation should not affect the spectral sensitivity, a requirement:

$$\left(\frac{\Delta G}{G}\right)^2 \ll \frac{1}{B\tau}, \tag{3.27}$$

has to be satisfied in the data integration time of τ(0.5 sec in SMILES). This requires the gain fluctuation of this kind be smaller than 0.03 % for the whole SMILES receiver. On the other hand, the gain variation of the second kind has to be less than 1 percent in a period of 53 seconds in order to achieve a 1-percent accuracy in the calibration of brightness temperatures.

3.3.4.3 Standing Waves

The third factor that can deteriorate the actual spectral sensitivity is standing waves in the submillimeter optics. The SMILES observations are performed in three successive steps with three different submillimeter inputs to the receiver: atmospheric emissions at numbers of consecutive tangent altitudes, reference-sky emissions at the altitude of 160 km or higher, and thermal emissions of the Calibration Hot-load (CHL). The AOS output voltages for these steps are described as follows:

$$V_{atm} = G_{sys} \cdot \{T_a(atm) \cdot M_{obs}(atm) + T_{sys}\}, \tag{3.28}$$
$$V_{ref} = G_{sys} \cdot \{T_a(ref) \cdot M_{obs}(ref) + T_{sys}\}, \tag{3.29}$$
$$V_{hot} = G_{sys} \cdot \{T_a(hot) \cdot M_{cal} + T_{sys}\}. \tag{3.30}$$

Here T_a is the antenna temperature evaluated at the input port of the receiver, and T_{sys} is the system noise temperature. G_{sys} is the system gain. $M_{obs}(atm)$, $M_{obs}(ref)$ and M_{cal} are power modulation factors due to standing waves. They are generated by a pair of reflections; one at the input port of the receiver and the other at some point in the submillimeter optics. The power modulation is due to the interference between an original incident wave and an additional one superimposed on it after a return trip along the optical path.

$$M_{obs} = \mid 1 + r_{obs} \cdot \exp(-j \cdot 2kL_{obs}) \mid^2 . \tag{3.31}$$

Here r_{obs} represents the relative strength of the superimposed wave, and L_{obs} is the distance between the two ends of the return trip ($k = 2\pi/\lambda$). On the other hand, the standing waves while the hot-load is observed are described by

$$M_{cal} = \mid 1 + r_{obs} \cdot \exp(-j \cdot 2kL_{obs}) + r_{cal} \cdot \exp(-j \cdot 2kL_{cal}) \mid^2 . \tag{3.32}$$

Here r_{cal} represents the relative strength of a superimposed wave that is returned from the hot-load, and L_{cal} is the distance between the input port of the receiver and the hot-load. The observed antenna temperature is derived from

$$T_a^{obs}(atm) = \frac{V_{atm} - V_{ref}}{V_{hot} - V_{ref}} \cdot \{T_a(hot) - T_a(ref)\} + T_a(ref). \tag{3.33}$$

Since M_{obs} and M_{cal} are frequency-dependent, this observed antenna temperature is also frequency-dependent, which makes a baseline ripple in the frequency spectrum.

There are several factors to determine the amplitude of standing waves. One is a difference (time variation) between $M_{obs}(atm)$ and $M_{obs}(ref)$. This difference can be generated by a thermal change of the physical distance between the two reflecting points in the optics. Keeping such temperature drift as small as 0.5 deg in 53 seconds could minimize this effect. The other factor originates from the insertion of the hot-load itself. The amplitude of this standing wave is mainly determined by the reflectivity of the hot-load. It has to be less than -50 dB to make r_{cal} lower than -60 dB. Recent experiments have demonstrated that the CHL meets such requirement (A.Murk, personal communication). The third factor is the variation of the system gain. Without such variations, the standing waves would decrease for lower atmospheric temperatures. The gain variation, however, makes the subtraction of T_{sys} incomplete in Eq. (3.33), which leaves some level of standing waves even for lower atmospheric temperatures.

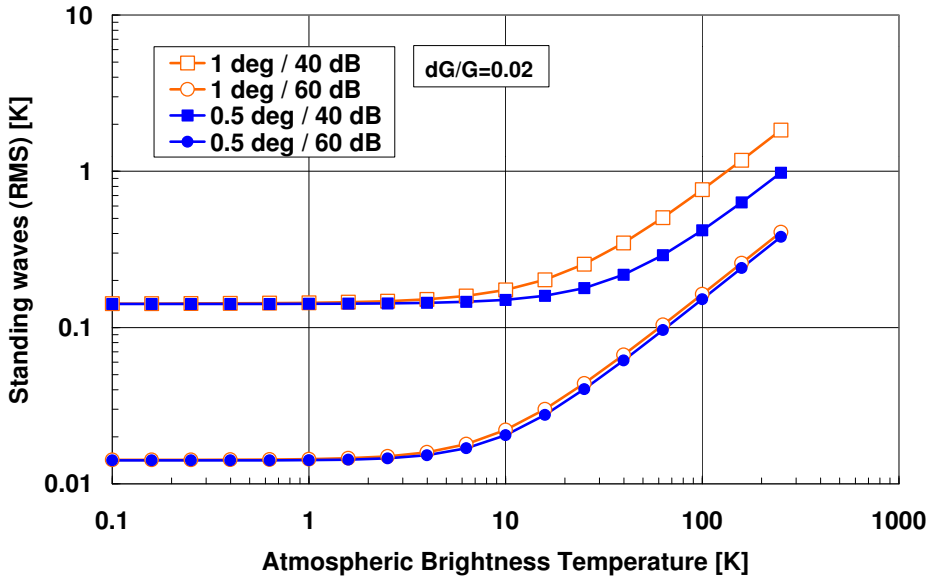

Figure 3.38 Estimated amplitude of standing waves as a function of atmospheric brightness temperature. Two cases for thermal stability in 53 seconds, and two cases for the strength of superimposed waves are calculated. The variation of the system gain is assumed to be 2 percent in 53 seconds.

The estimated amplitudes of standing waves are shown in Fig. 3.38. Two different cases are assumed with respect to thermal stability (1 deg or 0.5 deg in 53 seconds) and the relative level of superimposed waves (-40 dB or -60 dB for r_{obs}). r_{cal} is fixed at -60 dB, and the gain variation is assumed to be 2 percent. When r_{cal} is -60 dB, the amplitude (rms) of spectral ripples is less than 0.5 K for $T_a(atm)$ of 300 K, and linearly decreases for lower atmospheric temperatures, but remains around 0.02 K for temperatures lower than 10 K.

3.3.4.4 Differential Non-linearity of A/D Converter

The fourth factor we have to concern is differential non-linearity (DNL) of the analog-to-digital converter in the AOS. The incremental analog voltage, needed to give a step of smallest digital bit, is not exactly constant over the dynamic range. When a particular feature of this deviation is coupled with the frequency characteristic of the receiver gain, it results in a modulation of the signal spectra. This issue has been discussed in detail in section 3.3.3. With a measured feature of the DNL for the same type of analog-to-digital converter that is to be used for the AOS in SMILES, we have found this effect remains relatively small as shown in 3.41. But we have to keep it in mind that a temporal gain variation of 1 % is assumed there to estimate the DNL effect for the integrated data for a day.

3.3.4.5 Electromagnetic Interference

The fifth factor that could deteriorate the sensitivity of SMILES is electromagnetic interference. All the payloads aboard the International Space Station are requested to be compatible with the electromagnetic conditions specified in the requirement document (SSP-30237) [*NASA*, 1999]. Among categories with respect to the electromagnetic com-

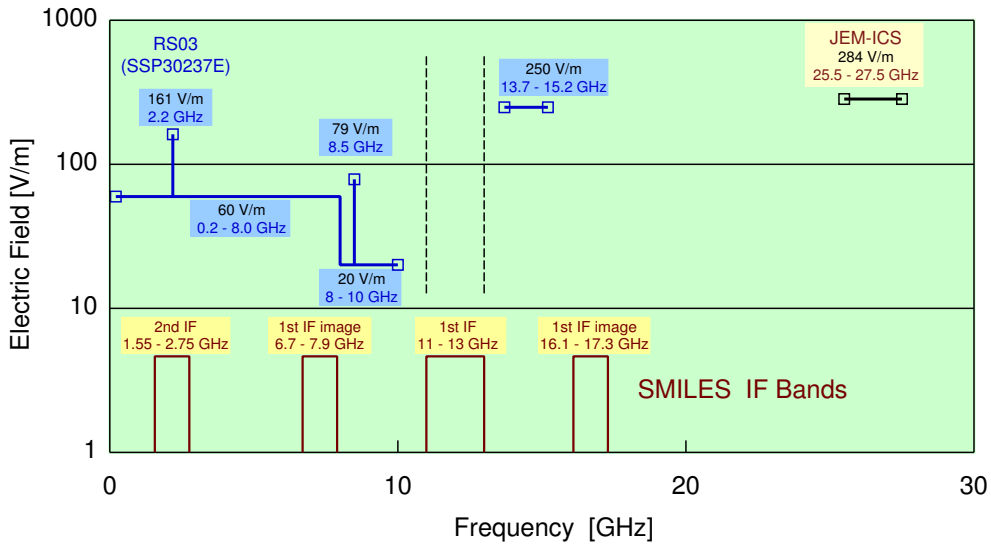

Figure 3.39 ISS environmental field. All the payloads aboard the ISS are requested to be compatible with the electromagnetic conditions specified in the requirement document (SSP-30237) [*NASA*, 1999].

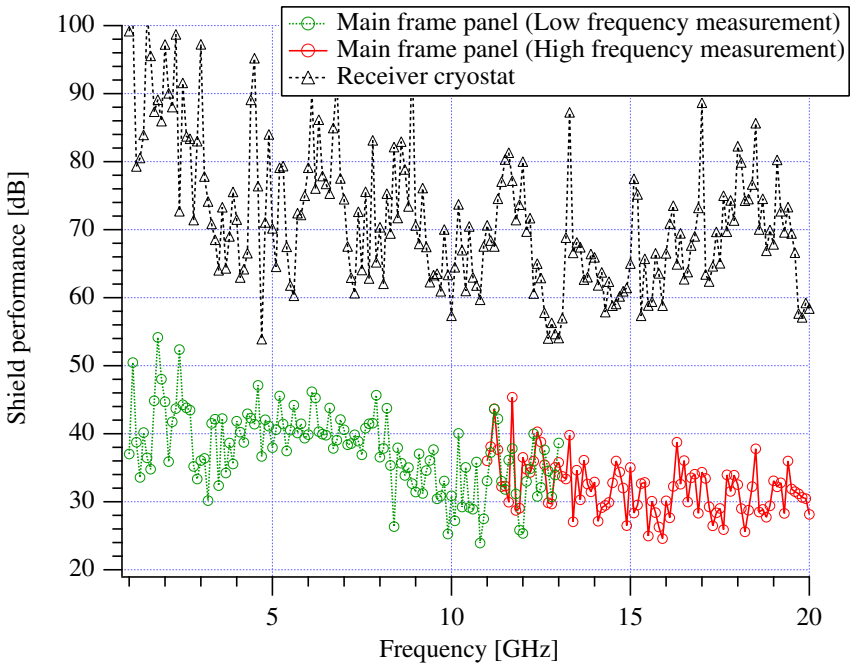

Figure 3.40 Shield performance. Thr measurement result demonstrates that the shielding performance of 20 dB and 50 dB has been achieved for the SMILES' structural model and the engineering model of the cryostat, respectively.

patibility (EMC) specifications, radiated susceptibility (RS) is most critical for SMILES to achieve its designed sensitivity. Figure 3.39 depicts radiated field specification levels as well as SMILES intermediate frequency (IF) band allocations. High electric fields must be anticipated at the SMILES' second IF band and a pair to the image bands according to the specification, while the first IF band (11 - 13 GHz) is not cited. To minimize the interference in such an environments, immunities of RF components shall be improved by paying special attention for their packaging. Our design target is not to observe, or recognize any spurious signal in a 'snap shot' (0.5 sec. integration) spectrum due to the electromagnetic interference. However, the ISS electromagnetic field specification is so harmful for the SMILES instrument to exhibit its full performance by itself. It is therefore essential for the payload instruments of SMILES being completely enclosed with an electromagnetic shield except for the antenna section. In particular, the most sensitive components, such as the SIS mixers and HEMT amplifiers, are to be tightly shielded by the cryostat. Figure 3.40 shows the shielding performance of the SMILES' structural panel and cryostat up to 26.5 GHz, demonstrating that the shielding performance of 20 dB and 50 dB have been achieved for the SMILES' structural model and the engineering model of the cryostat, respectively[*Miura et al.*, 2002; *Seta et al.*, 2002]. The submillimeter-wave signal from the antenna must be introduced to the cryostat without degrading the shielding capability. This will be accomplished by letting the submillimeter-wave beam pass through a small metallic tube (corrugated circular waveguide) that works as a cutoff filter against undesirable microwave field at 27 GHz or less.

Consolidating all the available data concerning the immunity of the instruments against the electromagnetic field radiation as well as the shielding performance so far achieved, we conclude that any spurious will not be observed in a snap shot spectrum under the

specified EMC conditions. As for the first IF frequency region, we estimate the field strength around the SMILES payload must be less than 2 V/m.

This frequency region is not cited in the EMC specification document because no transmitters emitting at this frequency are so far registered. Installation of new RF transmitter on the ISS can be a potential risk to prevent SMILES from appreciating its full sensitivity. Since this shall be approved through the evaluation of the EMC of the existent instruments aboard the ISS, we are requesting a control for 11-13 GHz emissions.

3.3.4.6 Overall Sensitivity

Overall sensitivity of SMILES is calculated in Figure 3.41 with the above factors except for the electromagnetic interference. For a unit data obtained in 53 seconds, the standard deviation of the noise in the spectral profile is expected to be about 0.7 K for brightness temperatures less than 20 K, but it increases gradually for higher temperatures due to standing waves. It will be about 1 K (rms) for brightness temperatures around 200 K, if the actual standing waves in orbit are of the level described above. In data processing on the ground, we will produce latitudinal zone-averaged spectral profiles to find the altitude-latitude relation of each species. The sensitivities of such zonal averaged data, generated by integrating unit data over all longitudes with a width of 5° in latitude, are also estimated for an integration period of 1 day and 1 month. The standard deviations will be reduced to 0.1 K for 1 day, and 0.03 K for 1 month, both for low brightness temperatures. They also increase for higher brightness temperatures due to the standing waves, which are not reduced by averaging unit data. Note that the sensitivity calculated here is for the spectral profiles with a frequency resolution of 2.5 MHz. If another kind of averaging, over several channels of the AOS, is available, the sensitivity will be improved even for a unit data at the price of lower frequency resolution.

3.3.5 Brightness Temperature Calibration

3.3.5.1 Calibration Scheme

If we take into account antenna responses in its wide-angle error pattern and thermal losses at antenna mirrors, the AOS output voltages are expressed by the next equations, corresponding to the three steps of data acquisition in a unit cycle (53 seconds).

$$\begin{pmatrix} V_{atm}/C_{aos}(G_{sys}+\Delta G_{sys}) \\ V_{ref}/C_{aos}G_{sys} \\ V_{hot}/C_{aos}G_{sys} \end{pmatrix} = \begin{pmatrix} T_{atm} & T_{err}+\Delta T_{err} & T_{mir}+\Delta T_{mir} & T_{sys}+\Delta T_{sys} \\ T_{ref} & T_{err} & T_{mir} & T_{sys} \\ T_{hot} & T_{hot} & T_{hot} & T_{sys} \end{pmatrix} \begin{pmatrix} K/L \\ (1-K)/L \\ (L-1)/L \\ 1 \end{pmatrix}. \quad (3.34)$$

It is assumed that some variations occur in G_{sys}, T_{err}, T_{mir} , and T_{sys} in a period between the time of atmospheric observations and that of intensity calibration. The meaning of each parameter is as follows:

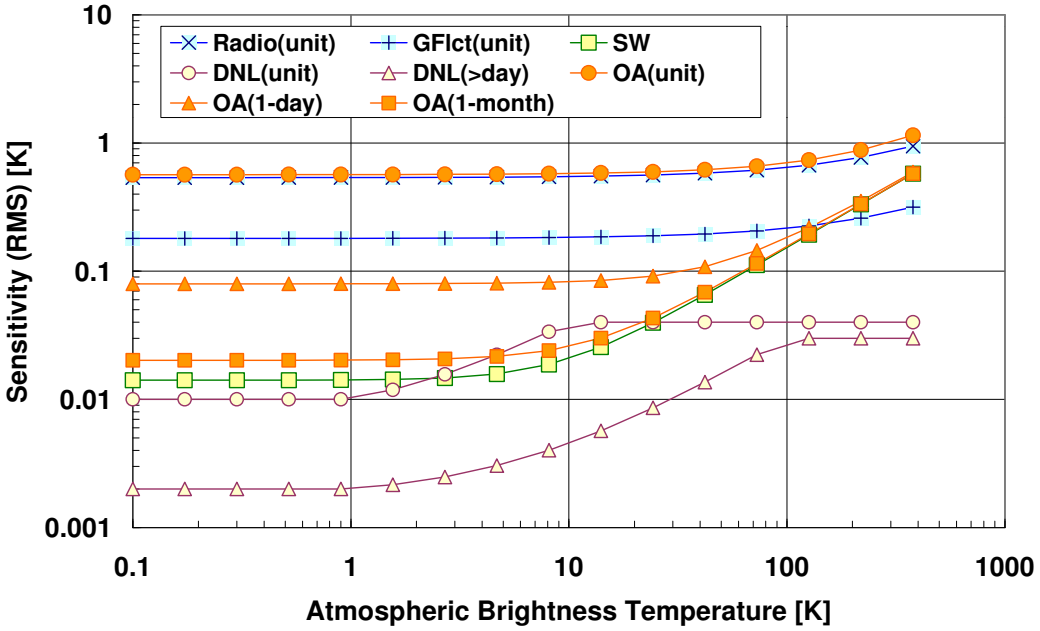

Figure 3.41 Overall Sensitivity: "Radio"; radiometric noise, "GFlct"; gain fluctuation, "SW"; standing waves, "DNL"; differential non-linearity of the analog-to-digital converter, "OA"; overall sensitivity obtained by rss (root-sum-squares). "unit" means the unit data obtained in 53 seconds. Standing waves are not reduced by averaging.

$V_{atm}, V_{ref}, V_{hot}$	;	Output voltages at the AOS corresponding to the atmosphere, reference sky, and hot-load, respectively (the zero-point offset is omitted for simplicity),
C_{aos}	:	Power-to-voltage conversion factor at the AOS,
G_{sys}	:	Total gain of the system that is from the calibrator to the AOS
K	:	Beam efficiency for the FOV defined by a 2.5×HPBW area,
L	:	Thermal losses at the antenna mirrors located before the calibrator,
T_{atm}, T_{ref}	;	Brightness temperatures integrated in the FOV corresponding to the atmosphere and reference sky, respectively,
T_{err}	:	Brightness temperature integrated outside the FOV,
T_{mir}	:	Brightness temperature of the antenna mirrors located before the calibrator, when they are assumed to be a black-body,
T_{hot}	:	Brightness temperature of the Calibration Hot-load (CHL),
T_{sys}	:	System noise temperature (SSB) evaluated at the calibrator.

With three observable voltages, V_{atm}, V_{ref}, and V_{hot}, we obtain an observable quantity, $VCAL$, that is basically free from the particular frequency characteristics in C_{aos}, G_{sys},

and the zero-point offset at the AOS.

$$VCAL = \frac{V_{atm} - V_{ref}}{V_{hot} - V_{ref}}. \tag{3.35}$$

With the measured value of $VCAL$, we obtain the atmospheric brightness temperature T_{atm} that is integrated in the FOV. However, there are several kinds of errors that will affect the derived value of T_{atm}.

At first, let us consider a simple case where no variations occur in G_{sys} , T_{err}, T_{mir}, and T_{sys}. We have

$$VCAL = \frac{T_{atm} - T_{ref}}{(T_{hot} - T_{ref}) + \frac{1-K}{K}(T_{hot} - T_{err}) + \frac{L-1}{K}(T_{hot} - T_{mir})}. \tag{3.36}$$

In this equation, the parameters have their real values at the time of observations. If we know and assume the values of T_{ref}, T_{err}, T_{mir}, T_{hot}, K, and L, then we can derive T_{atm} from this same equation. With these assumed values indicated with an asterisk, we obtain

$$VCAL = \frac{T^{obs}_{atm} - T^{*}_{ref}}{\left(T^{*}_{hot} - T^{*}_{ref}\right) + \frac{1-K^{*}}{K^{*}}(T^{*}_{hot} - T^{*}_{err}) + \frac{L^{*}-1}{K^{*}}(T^{*}_{hot} - T^{*}_{mir})}. \tag{3.37}$$

In this case, knowledge errors for these parameters will limit the accuracy of the derived value of T^{obs}_{atm}. This knowledge error can be evaluated by

$$\Delta T^{knw}_{atm} = T^{obs}_{atm} - T_{atm} = (\kappa - 1) \cdot T_{atm} \tag{3.38}$$

$$\kappa = \frac{T^{*}_{hot} + \frac{1-K^{*}}{K^{*}}(T^{*}_{hot} - T^{*}_{err}) + \frac{L^{*}-1}{K^{*}}(T^{*}_{hot} - T^{*}_{mir})}{T_{hot} + \frac{1-K}{K}(T_{hot} - T_{err}) + \frac{L-1}{K}(T_{hot} - T_{mir})}, \tag{3.39}$$

where T_{ref} and T^{*}_{ref} are assumed to be zero. Actually the antenna looks at the cosmic microwave background for the reference submillimeter input. Since the frequency of 640 GHz is in Wien's region of its 2.7-K spectrum, the brightness temperature expressed in Rayleigh-Jeans approximation is virtually zero.

As a second step, let us consider the effects of time variations of parameters between the time of atmospheric observations and that of intensity calibration. In this case, $VCAL$ is expressed as

$$VCAL = \frac{(T_{atm} - T_{ref}) + \Delta T^{var}_{atm}}{(T_{hot} - T_{ref}) + \frac{1-K}{K} \cdot (T_{hot} - T_{err}) + \frac{L-1}{K} \cdot (T_{hot} - T_{mir})}. \tag{3.40}$$

The error of derived T_{atm} due to variations is evaluated by

$$\Delta T^{var}_{atm} = \frac{1-K}{K} \cdot \Delta T_{err} + \frac{L-1}{K} \cdot \Delta T_{mir} + \frac{L}{K} \cdot \Delta T_{sys} + \frac{L}{K} \cdot \frac{V_{atm}}{C_{aos} G_{sys}} \cdot \frac{\Delta G_{sys}}{G_{sys}}. \tag{3.41}$$

Since the values of K and L are close to unity, and ΔT_{err} and ΔT_{mir} are likely of the order of 10 K, the first two terms should be smaller than the third and fourth terms.

$$\Delta T^{var}_{atm} \approx \Delta T_{sys} + (T_{atm} + T_{sys}) \frac{\Delta G_{sys}}{G_{sys}}. \tag{3.42}$$

This error is therefore the combination of a shift of the baseline in the frequency spectrum and a modification of the observed value of T_{atm}.

The third error factor on the derived T_{atm} is a residual nonlinear behavior of the system gain. The system gain is actually measured in orbit as a ratio of the difference of

two resultant output voltages to the difference of two input power levels: the hot-load and reference sky. The gain non-linearity is defined as a deviation of the actual output voltage from the expected value given by linear interpolation between the two measured points. This effect will be approximated by

$$\Delta T_{atm}^{GNL} = T_{atm} \cdot \frac{\Delta G_{sys}^{GNL}}{G_{sys}}. \tag{3.43}$$

This effect is therefore a modification of the observed value of T_{atm}.

For clarification, T_{atm} is not the real brightness temperature, $T_b(\theta_{atm})$, of the limb atmosphere exactly at a certain tangent altitude, but the one averaged in the FOV with a weighting function expressed by a near-axis response pattern of the antenna, $P(\theta)$.

$$T_{atm} = \frac{\int_{fov} T_b(\theta_{atm} + \theta) \cdot P(\theta) d\theta}{\int_{fov} P(\theta) d\theta}. \tag{3.44}$$

The role of the Level-1 data processing is to derive this averaged brightness temperature that should be as free as possible from system parameters and effects of the wide-angle response pattern. On the other hand, the effect of the near-axis response pattern is strongly coupled with the altitude distribution of the molecular mixing ratio itself, which should be properly resolved in the Level-2 processing.

3.3.5.2 Calibration Accuracy

We estimate the calibration accuracy of T_{atm} in the following. Error factors to be estimated are the knowledge error, gain variation, gain non-linearity, standing waves, differential non-linearity, and radiometer noise. To estimate the effect of knowledge errors quantitatively, let us assume reasonable values and the extent of knowledge errors for the parameters used in Eq. (3.38).

K :	0.92	$\pm$ 0.02	(to be evaluated by the ground measurements)
L :	0.5 dB	$\pm$ 0.2 dB	(to be evaluated by the ground measurements)
T_{err} :	100 K	$\pm$ 30 K	(to be evaluated by the ground measurements)
T_{mir} :	270 K	$\pm$ 10 K	(to be measured in orbit)
T_{hot} :	300 K	$\pm$ 1 K	(to be measured precisely in orbit)

Expected error in the derived value of T_{atm}, calculated by Eq. (3.38), is shown in Figure 3.42 as a function of its assumed value. This error is proportional to the brightness temperature, and its relative value is less than 3 percent (rms). The knowledge error is the largest one among various error factors considered here.

Secondly, the calibration accuracy is affected by temporal variation of the system gain and system noise temperature. It is expressed by Eq. (3.42). If we can remove the effect of the baseline shift (uncertainty) from the original observed data, the calibration error of the brightness temperature will be proportional to its value. In Figure 3.42, it is shown as "GTV", which is about 1 percent (rms) corresponding to the gain variation of $\pm$2 percent in maximum amplitude.

Thirdly, the calibration accuracy is affected by the gain non-linearity. The effect expressed by Eq. (3.43) is depicted as "GNL" in Figure 3.42 for the case of residual non-linearity of $\pm$1 percent in maximum amplitude.

Errors due to other factors such as standing waves, differential non-linearity, and radio noise are also included in Figure 3.42, which are shown a"SW", "DNL", and "Radio". In

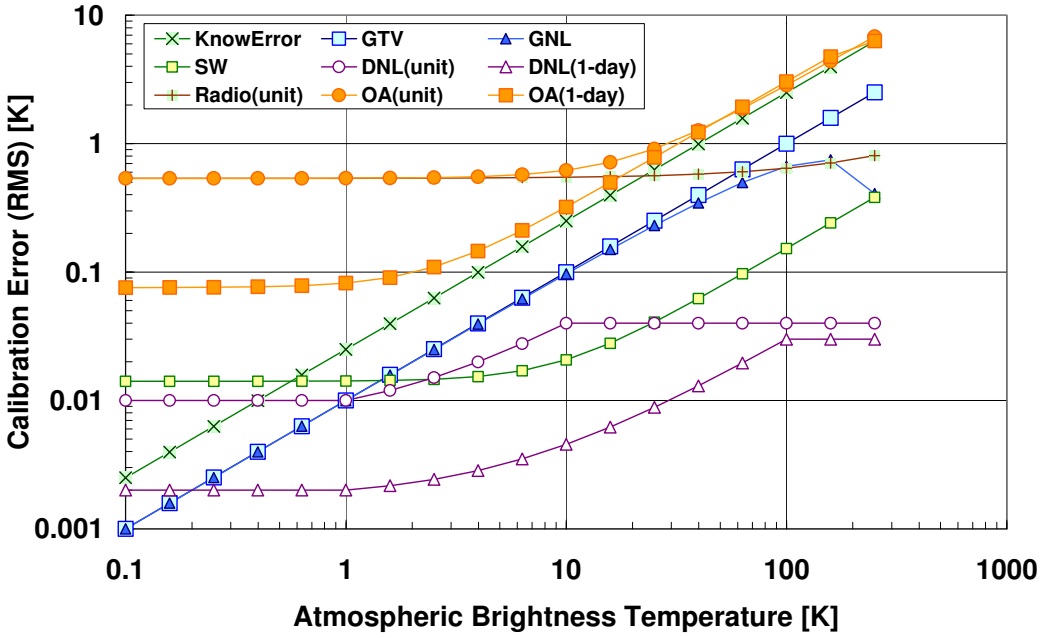

Figure 3.42 Calibration accuracy of the brightness temperature: "KnowError"; knowledge error, "GTV"; time variation of the system gain, "GNL"; non-linearity of the system gain, "SW"; standing waves, "DNL"; differential non-linearity of the analog-to-digital converter of the AOS, "Radio"; radiometer noise, and "OA"; overall error.

conclusion, the overall error is about 0.8 K (rms) for atmospheric brightness temperatures lower than 20 K, and about 3 percent (rms) for higher temperatures. The radiometer noise dominates in lower temperatures, and the knowledge error does in higher temperatures. For the zonal averaged data in 1 day, the overall calibration error will decrease as the radiometer noise decreases for atmospheric temperatures lower than 20 K. But this is also limited by the knowledge error for temperatures between 2 K and 20 K.

We have to keep in mind that Figure 3.42 does not include the uncertainty of the spectral baseline, i.e. the level of zero emissions. As shown in Eq. (3.42), time variations of the system gain and system noise temperature can contribute to a large shift of the baseline. It is difficult to evaluate its amount precisely, but it may reach up to ± 20 K, if both $\Delta T_{sys}/T_{sys}$ and $\Delta G_{sys}/G_{sys}$ are ± 2 percent. This uncertainty of the baseline will not affect the accuracy of the observed emissions with a line-width that is narrow enough compared with the bandwidth (1.2 GHz) of the AOS. However, this uncertainty will limit the capability of SMILES to derive some parameters, such as concentration of water vapor in the atmosphere, from the absolute level of its brightness temperature, because of its flat spectrum.

3.4 Conclusion

Chapter 3 has dealt with instrumental capabilities of SMILES. Emphasis is put on the aspects of those that are directly coupled to the quality of observational data. We have investigated SMILES performances with respect to the field of view as well as the spectral regions and sensitivity. To conclude this chapter, we put two tables for description of SMILES mission instruments (Table 3.16) and for a summary of those capabilities (Table 3.17). Note that some figures in the latter table are still under investigation and subject to future revisions.

Table 3.16 Description of SMILES Mission Instruments

Instruments	Description
Submillimeter Antenna	
Type	Offset Cassegrain antenna shaped for an elliptical beam
Size of main reflector	400 mm (Vertical) × 200 mm (Horizontal)
Azimuth	Fixed to 45-deg north with respect to the ISS forward direction
Elevation	Movable from $-40°$ to $+5°$
Intensity calibration	With an ambient-temperature load and cold sky
Sumillimeter Receiver	
Type	Cryogenically cooled heterodyne receiver
Submillimeter mixer	SIS mixer with Nb/AlOx/Nb junctions operating at 4.5 K
LO source	Gunn diode oscillator and frequency multiplier
First-stage IF amplifier	HEMT amplifier operating at 20 K
Cryogenics	Two-stage Stirling cooler plus Joule-Thomson cooler
Sideband separation	Modified Martin-Puplett interferometer
IF Amplification Section	
Type	Down conversion and amplification
Switching	Switching to control signal flow into AOS units
Reference frequency	Reference CW generation for AOS frequency calibration
AOS	
Type	Radio spectrometer based on acouto-optical interaction
Light deflector	LiNbO3-based Bragg's cell
Laser	Laser diode emitting at 785 nm
Detector	CCD linear array
Star Tracker	
Type	Image mapping and comparison with a star catalogue
Field of view	$18.4° \times 13.4°$
Star catalogue	Hipparcos data containing 12200 stars

Table 3.17 Summary of SMILES Instrumental Capabilities

Parameters	Characteristics
Spatial Coverage	
Tangent-point Height	−10 km to 60 km (minimum)
Latitude	65°N to 38°S (nominal)
Data Sampling Interval	Around 360 km along the orbit
Data Sampling Speed	105 sets of data per orbit
Orbital Period	About 93 minutes
Accuracy of Height Determination	
Bias Error	About 0.76 km (rms)
Random Error	About 0.34 km (rms) [after calibrated for a beam-offset error]
Resolution of Tangent-point Height	
Effective Beam-width (HPBW)	0.096° (3.5-4.1 km in height scale)
Sampling Interval	0.056° (2.1-2.4 km in height scale) [for the ISS altitude of 407 km]
Frequency Coverage	
Band-A	624.32 — 625.52 GHz
Band-B	625.12 — 626.32 GHz
Band-C	649.12 — 650.32 GHz
Major Molecular Species to be Measured(*)	
Band-A	O_3, O_3-isotopes, $H^{37}Cl$, H_2O_2, $HO^{35}Cl$, HNO_3, SO_2, ^{81}BrO
Band-B	O_3, O_3-isotopes, $H^{35}Cl$, HO_2, HNO_3, SO_2, $O^{35}ClO$
Band-C	^{35}ClO, O_3-isotopes, HO_2, HNO_3, SO_2, ^{81}BrO
Sensitivity for Atmospheric Brightness Temp.	
For Unit Data	About 0.7 K (rms) for $T_b < 20$ K
(Acquired in every 0.5 sec)	About 1.0 K (rms) for $T_b = 200$ K
For Daily 5-deg Zonal Avg. Data	About 0.1 K (rms) for $T_b < 20$ K
(Integrated over all longitudes)	About 0.3 K (rms) for $T_b = 200$ K
Accuracy for Atmospheric Brightness Temp.	
For Unit Data	About 1 K (rms) for $T_b < 20$ K
	About 3 % (rms) for $T_b > 20$ K
For Daily 5-deg Zonal Avg. Data	About 0.1 K (rms) for $T_b < 2$ K
	About 3 % (rms) for $T_b > 2$ K
Baseline Uncertainty	Less than ±20 K
Spectrometer Capabilities	
Frequency Resolution (FWHM)	1.8 MHz
Channel Separation	0.8 MHz per channel
Number of Channels	1728 channels per a CCD unit

*Only two bands are operational at a time.

References

Fujii, Y., K. Kikuchi, J. Inatani, Y. Irimajiri, M. Seta, S. Ochiai, T. Manabe, H. Masuko, T. Noguchi, K. Narasaki, S. Tsunematsu, and T. Shirota, Space-borne 640-GHz SIS Receiver Based on 4-K Mechanical Cooler, *UV, Optical, and IR Space Telescope and Instruments, Proceedings of SPIE, 4013,* 90—99, 2000.

Inatani, J., T. Noguchi, S. C. Shi. K. Miyazawa, H. Masuko. S. Ochiai, Y. Irimajiri, M. Kyoya, K. Narasaki, S. Tsunematsu, M. Murakami, and D. Okamoto, A Submillimeter SIS Receiver Cooled by a Compact Stirling-JT Refrigerator, Eighth International Symposium on Space Terahertz Technology, 273—280, 1997.

Inatani, J., S. Ochiai, T. Manabe, M. Seta, R. Wylde, and D. H. Martin, A New Configuration of the Martin-Puplett Interferometer with Low-Reflection, IEEE Seventh International Conference on Terahertz Electronics Proceedings, 260—263, 1999.

International Telecommunication Union, *ITU-R Reccomendations,* Rec. ITU-R 835-2, 1997 P Series-Part I, Geneve, 1997.

Manabe, T., Effects of Atmospheric Refraction on Limb Sounding from JEM/SMILES, available at http://www.crl.go.jp/ck/ck321/smiles/refrac.pdf, 1999.

Manabe, T., Effects of Atmospheric Refraction on Limb Sounding from JEM/SMILES –Part II–, available at http://www.crl.go.jp/ck/ck321/smiles/refrac/refrac.html, 2000.

Miura, T., T. Nishibori, J. Inatani, and JEM/SMILES Mission Team, Measurement of Shield Performance of JEM/SMILES Payload, Proceedings of the 2002 IEICE General Conference, (Communications 1), 396 (B-4-47), 2002 (in Japanese).

Martin, D. H., Polarizing (Martin-Puplett) interferometric spectrometers for the near- and submillimeter spectra, in *Infrared and Millimeter Waves,* vol. 6, K. J. button, Ed. New York: Academic Press, 1982, pp. 65—148.

NASDA, *Introductory Guidebook for JEM Exposed Facility Potential Users,* JBX-98079, National Space Development Agency of Japan, 1998.

NASA, *International Space Station User's Guide Release 2.0,* National Aeronautics and Space Administration, available at http://spaceflight.nasa.gov/station/reference/issug/ISSUG1-11.pdf, http://spaceflight.nasa.gov/station/reference/issug/ISSUG12-34.pdf, http://spaceflight.nasa.gov/station/reference/issug/ISSUG35-50.pdf.

NASA, *Space Station Electromagnetic Emission and Susceptivility Requirements,* SSP 30237, Revision E, September, 1999.

NASA, *System Specification for the International Space Station,* SSP41000R, March 20, 2000.

Ozeki, H., Y. Kasai, S. Ochiai, S. Tsujimaru, J. Inatani, H. Masuko, C. Takahashi, L. Mazuray, and C. Rosolen, Submillimeter-wave Spectroscopic Performance of JEM/SMILES, SPIE Second International Asia-Pacific Symposium on Remote Sensing of the Atmosphere, Environment, and Space, Sendai, Japan, October 9–12, 2000.

Seta, M., T. Miura, T. Manabe, S. Tsunematsu, T. Nishibori, and J Inatani, 'Evaluation of Electromagnetic Shielding Capability of a Spaceborne Cryostat for a Sensitive Receiver,' Proceedings of the 2002 IEICE General Conference, (Communications 1),397 (B-4-48), 2002 (in Japanese).

Treder, A. J., *Space Station GN&C Overview for Payloads, Space Technology and Applications International Forum-1999,* 49-57, 1999.